Journal of Structural Geology 192 (2025) 105356

Contents lists available at ScienceDirect

Journal of Structural Geology

journal homepage: www.elsevier.com/locate/jsg

Displacement analysis of basin-scale reactivated normal faults: Insights from the West Netherlands Basin

Annelotte Weert [a,*], Giovanni Camanni [a,b], Marco Mercuri [c], Kei Ogata [a,d], Francesco Vinci [e,f], Stefano Tavani [a,g]

[a] Dipartimento di Scienze della Terra, dell'Ambiente e delle Risorse (DiSTAR), Università degli Studi di Napoli 'Federico II', Naples, 80126, Italy
[b] Dipartimento di Scienze Chimiche e Geologiche, Università di Modena e Reggio Emilia, Modena, 41125, Italy
[c] Dipartimento di Scienze della Terra, Sapienza Università di Roma, Rome, 00185, Italy
[d] Dipartimento di Scienze della Terra, dell'Ambiente e della Vita (DiSTAV), Università di Genova, Genova, 16132, Italy
[e] Shell Global Solutions International B.V., the Hague, 2596HP, the Netherlands
[f] PanTerra Geoconsultants B.V., Leiderdorp, 2352BZ, the Netherlands
[g] Consiglio Nazionale delle Ricerche, IGAG, Rome, 00185, Italy

ARTICLE INFO

Keywords:
Displacement-distance diagrams
Fault reactivation
Extensional tectonics
Syn-kinematic sediments
Basin inversion
Fault linkage
Fault growth

ABSTRACT

Displacement-distance diagrams are valuable for studying fault interactions and growth. Examples of displacement patterns for faults that underwent multiple reactivation events are limited. This study presents along-strike and along-dip displacement-distance diagrams for nine basin-scale faults from the West Netherlands Basin, which has experienced multiple phases of displacement. The diagrams were derived from 3D seismic reflection data, covering 2300 km^2 and 6 km in depth. Due to the dataset size, we developed a semi-automated workflow to map faults, reduce noise, and generate displacement-distance diagrams. To determine the effects of both multiphase rifting and transpressive basin inversion on fault growth, we studied four faults only recording extensional events and five faults that also experienced inversion. We observed distinctive along-dip displacement patterns, characterized by piecewise curves, identifying pre-, syn-, and post-rift phases of fault growth, as well for a later inversion event. The shape of lateral displacement patterns suggests quasi-fixed lateral fault tips throughout the fault's history and faults developing their lateral lengths early, with later reactivation mainly increasing their vertical extent while accumulating displacement. In addition to improving our understanding of how faults grow through multiple reactivations, these results may provide insights into the growth-history of faults in other inverted rift basins world-wide.

1. Introduction

Fault displacement patterns provide valuable insights into the behaviour of faults (e.g., Walsh and Watterson, 1988, 1989; Hedlund, 1997; Nicol et al., 2017, 2020 and references therein), making them essential in structural geology, earthquake geology, seismology, and resource exploration (e.g., Hughes and Shaw, 2014; Michie and Braathen, 2024). Among other aspects, they provide insights into the growth of individual faults (Nicol et al., 2017; Torabi et al., 2019; Nicol et al., 2020 and references therein) and how they interact with adjacent faults in terms of fault displacement accumulation (Marchal et al., 2003; Agosta and Aydin, 2006; Kristensen et al., 2008; Tondi et al., 2012; Nixon et al., 2014; Seebeck et al., 2015; Nicol et al., 2017; Childs et al., 2017; Lăpădat et al., 2017; Delogkos et al., 2020; Roche et al., 2021; Deng et al., 2020; Alghuraybi et al., 2023; Camanni et al., 2023a).

In 3D, an 'ideal' isolated dip-slip fault cutting through pre-kinematic layers produces concentric, nearly elliptical displacement contours (Fig. 1a), with the largest fault throw situated at the centre of the fault plane, radially diminishing towards the fault tips (Rippon, 1984; Barnett et al., 1987; Walsh and Watterson, 1988; Nicol et al., 1996; Needham et al., 1996). Strike and dip sections through these elliptical contours produce triangular- or bell-shaped graphs, where the slope of the curve (s) corresponds to the gradient of diminishing displacement toward the fault tips (Walsh and Watterson, 1989); these gradients are particularly high across fault relay zones (Camanni et al., 2023b and references therein), where displacement is transferred between adjacent fault

* Corresponding author.
E-mail address: annelotteweert@gmail.com (A. Weert).

https://doi.org/10.1016/j.jsg.2025.105356
Received 30 September 2024; Received in revised form 29 January 2025; Accepted 31 January 2025
Available online 4 February 2025

segments (e.g., Peacock and Sanderson, 1991; Childs et al., 1995; Nicol et al., 2017; Delogkos et al., 2020).

The complexity of displacement-distance diagrams increases when initially isolated, adjacent fault segments become linked during growth and form throughgoing structures. In these cases, saddles on the displacement profile for the final throughgoing fault and at segment boundaries have been used to discriminate between two models of fault growth: the isolated model and the constant-length (or coherent) model (Childs et al., 1995, 2017; Walsh et al., 2002; Giba et al., 2012; Nicol et al., 2017, 2020; Rotevatn et al., 2019). In the isolated model, faults originating as separate segments eventually link as they grow, due to an increase in both length and displacement. The isolated model results in a displacement minimum in the displacement profile of the throughgoing fault (Fig. 1b). In contrast, the constant-length (or coherent) model includes faults that reached their full length early on, and with further growth they exclusively accumulate displacement, without extending in length. The constant-length model is generally not associated with a displacement minimum in the displacement profile of the throughgoing fault.

Displacement patterns can be further complicated when syn-kinematic sedimentation and/or erosion occur, both on isolated and linked faults, as it causes a significant increase in displacement on along-strike and along-dip diagrams at the base of the syn-kinematic interval. On growth faults, for example, displacement is expected to be distributed asymmetrically on the fault surface(s) and on along-dip slip profiles, with maximum slip values being located near the base of the faulted sequence, generally diminishing upward (e.g., Giba et al., 2012; Jackson et al., 2017, Fig. 1c).

Even more complex is the situation where faults are reactivated multiple times, in some situations even with opposed senses of movement (e.g., extensional faults inverted during basin inversion). In the latter cases, discriminating between the different processes that shaped the displacement-distance diagram is challenging, and, to date, only a few examples are reported in the literature (Tvedt et al., 2013; Duffy et al., 2015; Deng et al., 2017; Reilly et al., 2017; Torabi et al., 2019). This study aims to enhance the understanding of fault growth by providing examples of distinctive, first-order features that facilitate the identification of these complex scenarios on displacement-distance diagrams. Hence, we aim to improve the accuracy of translating along-dip and along-strike displacement-distance diagrams into the vertical and lateral growth modes of polyphase faults.

This study provides new insights into fault growth and presents a time-efficient workflow for the creation of displacement-distance diagrams. The workflow integrates manual and automatized steps and is calibrated to consider uncertainties linked to basin-scale fault mapping, ensuring data quality. We believe that such a workflow could be applied to industrial projects, where it would represent a more efficient alternative to standard solutions.

Using a 3D seismic reflection dataset, we show the along-strike and along-dip displacement-distance patterns for nine faults in the West Netherlands Basin (WNB). With a poly-phase tectonic history, at least two rifting phases and one positive inversion event are recognized in the WNB (e.g., Weert et al., 2024). Specifically, four of the nine studied faults experienced only (multiphase) extensional activity, while the other five also underwent reverse reactivation (i.e., inversion). These faults permit the study of the effects of multiple extensional phases on

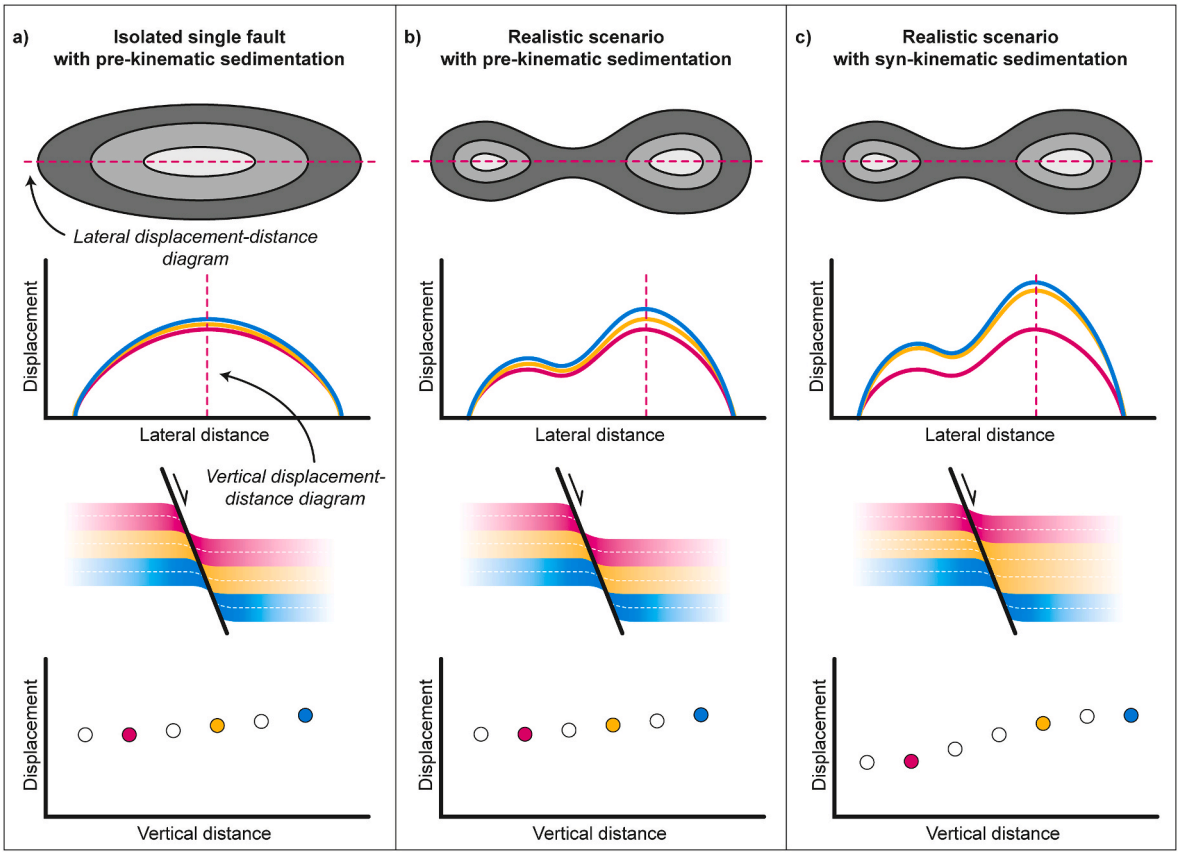

Fig. 1. Three scenarios for faults: (a) An isolated single fault with pre-kinematic sedimentation; (b) Two linked faults that developed after sedimentation; (c) Three connected faults that developed during sedimentation of the orange layer. All three scenarios show, from top to bottom: a structural contour map, an along-strike displacement distance diagram, a schematic section across-dip in 2D, and an along-dip displacement distance diagram. The displacement distance diagrams show the relationship for each sedimentary layer (pink, orange and blue). For the along-dip diagram, the white dashed layers are included in their displacement distance diagram. The pink line on the structural contour map and in the 2D schematic section indicates the transect illustrated on the displacement-distance diagrams. (For interpretation of the references to colour in this figure legend, the reader is referred to the Web version of this article.)

fault displacement patterns and also to discriminate the effects of subsequent positive inversion. The key features observed in this study are also expected to be applicable in explaining the growth history of faults in other inverted rift basins worldwide.

2. Geological setting

The West Netherlands Basin (WNB) is situated below the western part of the Netherlands (Fig. 2). The basin developed on a former Paleozoic basin, inheriting its NW-SE elongated structural trend (Ziegler, 1992; van Balen et al., 2000; Worum et al., 2005) and underwent a complex, multiphase evolution during the Mesozoic (van Wijhe, 1987; Racero-Baena and Drake, 1996; van Balen et al., 2000; Weert et al., 2024). Initial opening likely occurred in the Triassic under a NE-SW extensional regime, resulting in the development of NW-SE-elongated fault-bounded horst-and-grabens. The last, and strongest, rifting pulse occurred during the Late Jurassic and Early Cretaceous under an ENE-WSW extensional regime; the horst-and-grabens evolved into narrow lozenge shaped half grabens, bounded by NW-SE and NNW-SSE striking faults (Weert et al., 2024). Successively, the African-European convergence induced a compressional tectonic regime by the Late Cretaceous (Kley and Voigt, 2008), strongly affecting the WNB. The pre-existing normal faults became inverted, characterized by reverse oblique-slip senses of movement (Racero-Baena and Drake, 1996). In some circumstances, buttressing occurred and caused general uplift and erosion, increasing in magnitude towards the NE part of the basin (Worum and van Wees, 2017; Weert et al., 2024). Inversion-related compression would continue until the Miocene, further uplifting the NE sector of the WNB and causing general erosion of the entire basin (Worum and Michon, 2005; Kley, 2018; Weert et al., 2024).

This study focuses on the Jurassic-Cretaceous faulted, sedimentary cover (Fig. 3). The succession includes the open-marine deposits of the Early to Middle Jurassic Altena Group, the fluvial-deltaic sediments of the Late Jurassic to Early Cretaceous Nieuwerkerk Formation, the coastal to open-marine clastics of the Early Cretaceous Rijnland Group, and the marine carbonates of the Late Cretaceous Chalk Group (van Adrichem Boogaert and Kouwe, 1993; TNO-GDN, 2024).

3. Data

This work is based on publicly available 3D depth converted seismic reflection cubes (L3NAM2012AR and L3NAM2016CR), downloaded from https://www.nlog.nl/datacenter/(last accessed on February 5, 2024). The datasets cover a total of 2300 km^2 from the on- and offshore WNB (Fig. 2), and extend to a depth of 6 km. Both datasets are reprocessed from the L3NAM1990C 3D seismic survey, and have a continuous numbering in inlines and crosslines. L3NAM2016CR covers inlines 1430–3210 and crosslines 2300–3980, and L3NAM2012AR includes inlines 2500–5178 and crosslines 2273–3987. Inlines 2500–3210 are present in both datasets, facilitating a smooth interpretation of analogous horizons across datasets. More technical details and information about the reprocessing can be found in the public processing reports that accompany the 3D seismic datasets on nlog.nl.

4. Methods

Structural analysis was built upon seismic interpretation performed in Petrel 2020.3 software. We used a standard workflow for interpreting seismic datasets in extensional settings (e.g., O'Sullivan et al., 2022). The faults' and horizons' reconstruction is based on the seismic interpretation done for the L3NAM2012AR seismic cube, published and described by Weert et al. (2024), and extended for the L3NAM2016CR seismic dataset (Fig. 3). A 25x25 grid of cross-lines and inlines was used to guide mapping and ensure geological consistency. In detail, five superposed seismic horizons were mapped for both datasets, selected for their distinct seismic facies or notable tectono-stratigraphic characteristics, such as unconformities. The base of the Late Cretaceous Chalk Group is marked by a bright, clearly trackable peak. It lies mostly conformable on underlying strata, with some local unconformities. The base of the Early Cretaceous Rijnland Group is defined by a minor, less distinct peak. Within the sub-basins, well tops were used to interpret the base of the Rijnland Group, as indicated in Weert et al. (2024). The base of the Late Jurassic Nieuwerkerk Formation is a bright, trackable trough, which lies conformably on the Altena Group, though some local unconformities are present. The bases of the Middle Jurassic Posidonia Shale Formation and Early to Middle Jurassic Altena Group are easily recognizable bright troughs (Fig. 3).

After producing the surfaces from the mapped horizons, the edge detection surface attribute in Petrel was used (Fig. 4). This attribute detects surface areas with a subtle change in elevation, aiding in the identification of distinct sharp edges (e.g., Daniilidis et al., 2016), returning values ranging between 0 and 100%. Importantly for this work, areas with a value below 20% were recognized as fault planes and removed from the original surfaces, resulting in a surface with gaps corresponding to locations of the fault surface. In the case of the base of the Chalk Group, which is mostly unaffected by faults, the edge detection surface attribute does not allow to distinguish between steeply dipping monoclines and fault planes.

For the along-strike fault displacement analysis, the surfaces were converted into a dense point mesh (roughly 74 points/km^2) and imported into Petroleum Experts Move 2017.2 software (Fig. 4). Here, the point mesh was turned back into a surface using the Delauney triangulation method for surface creation, which, given the absence of steeply-dipping to overturned strata, returned a smooth and reliable surface. In the surfaces produced by Move, the earlier created gaps for the fault planes are fixed, and the fault planes are stripped from noise and secondary structures. From these new surfaces, individual fault plane surfaces were produced for the selected nine faults. To generate the along-strike displacement-distance diagrams, both the surfaces and fault planes were inserted in Move's Fault Analysis module (Fig. 4). As the surfaces now have smoothed fault planes, the Fault Analysis tool can quickly identify the footwall and hanging wall cut-off lines, from which the along-strike displacement-distance diagrams are derived. The strip close to the fault is excluded from the analysis, wherefore the cut-off lines are obtained by extending the strata from a certain distance as a straight line. Such a procedure has the advantage of capturing the total displacement, which includes both discrete and continuous deformation (i.e., folding, dragging, and bed rotations; Nicol et al., 2002; Delogkos et al., 2017). This semi-automatic method generally overestimates the stratigraphic elevation of the upper tip of the faults, which has the advantage of incorporating folding ahead of the fault into the displacement-distance diagrams. For example, manual seismic interpretation of inverted faults shows the presence of the upper fault tip below the base of the Chalk Group (Fig. 3), whereas the presented method here extends the upper fault tip upward, up to the base of the Chalk. The produced patterns were visually checked for inconsistencies, comparing them with the seismic display of the fault in Petrel. Artifacts were edited manually, securing the best representation of each fault.

To enhance the interpretation of the along-strike displacement-distance patterns, along-dip displacement-distance diagrams were produced for locations within the along-strike diagrams that show a displacement maxima. These along-dip displacement-distance diagrams illustrate how fault displacement (throw) changes along the vertical length of a fault. The diagrams represent proxies for the accumulation of displacement through time, which is indicated by the displacement gradient. The diagrams show the distance from the fault tip to specific layers in the hanging wall or footwall on the x-axis, and the fault throw on the y-axis. In the seismic data, the upper fault tips are better visible and the hanging wall generally has a thicker sediment stack. Therefore, the displacement gradient was obtained by measuring the distance from the upper fault tip to each selected horizon in the hanging wall. The fault

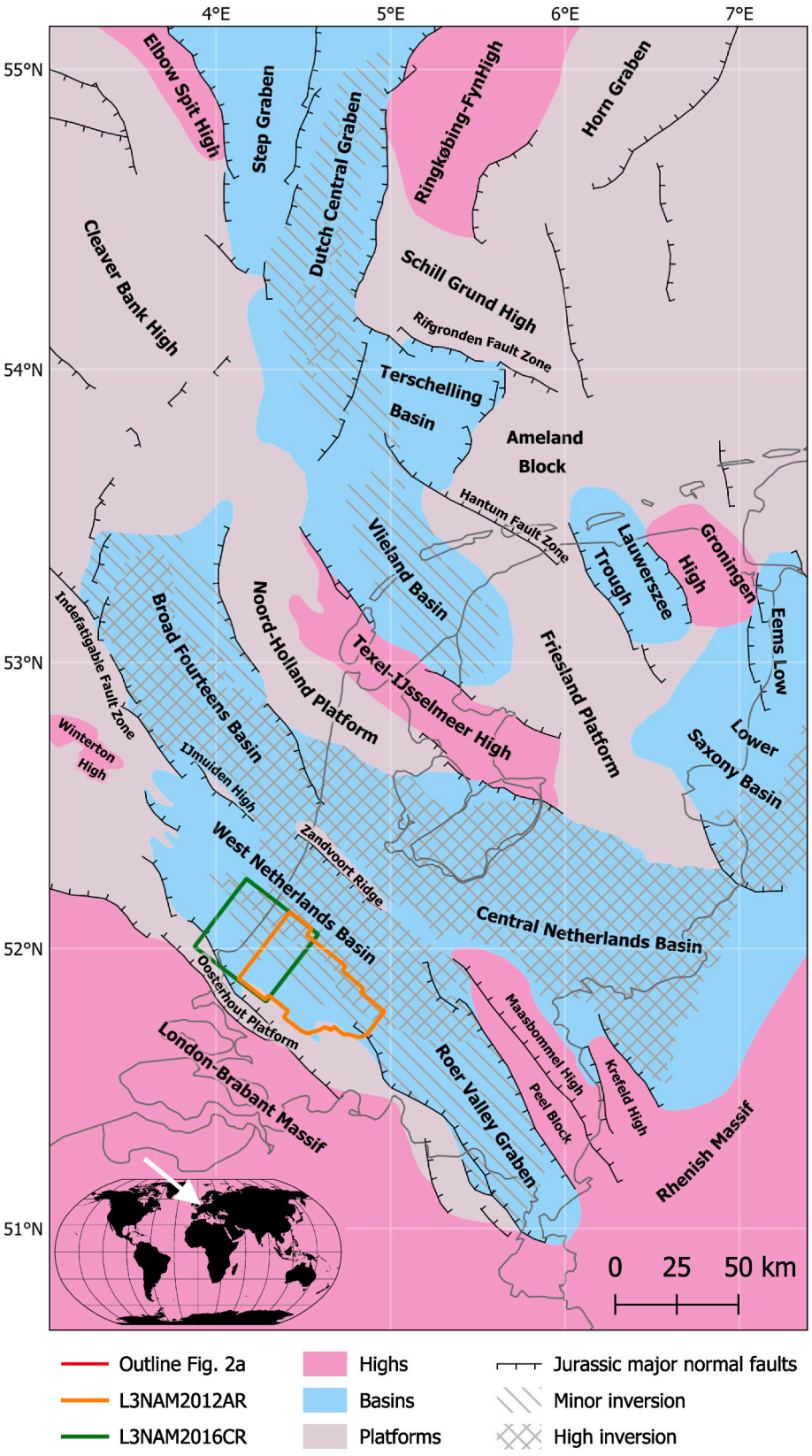

Fig. 2. Principle tectonic structures of the Netherlands and the eastern North Sea during the Jurassic. The areas affected by the Late Cretaceous and Cenozoic basin inversion are marked. The 3D seismic reflection datasets are indicated in orange and green. This map was updated from Weert et al. (2024) and produced by combining the maps from Wong et al. (2007) and Kombrink et al. (2012). (For interpretation of the references to colour in this figure legend, the reader is referred to the Web version of this article.)

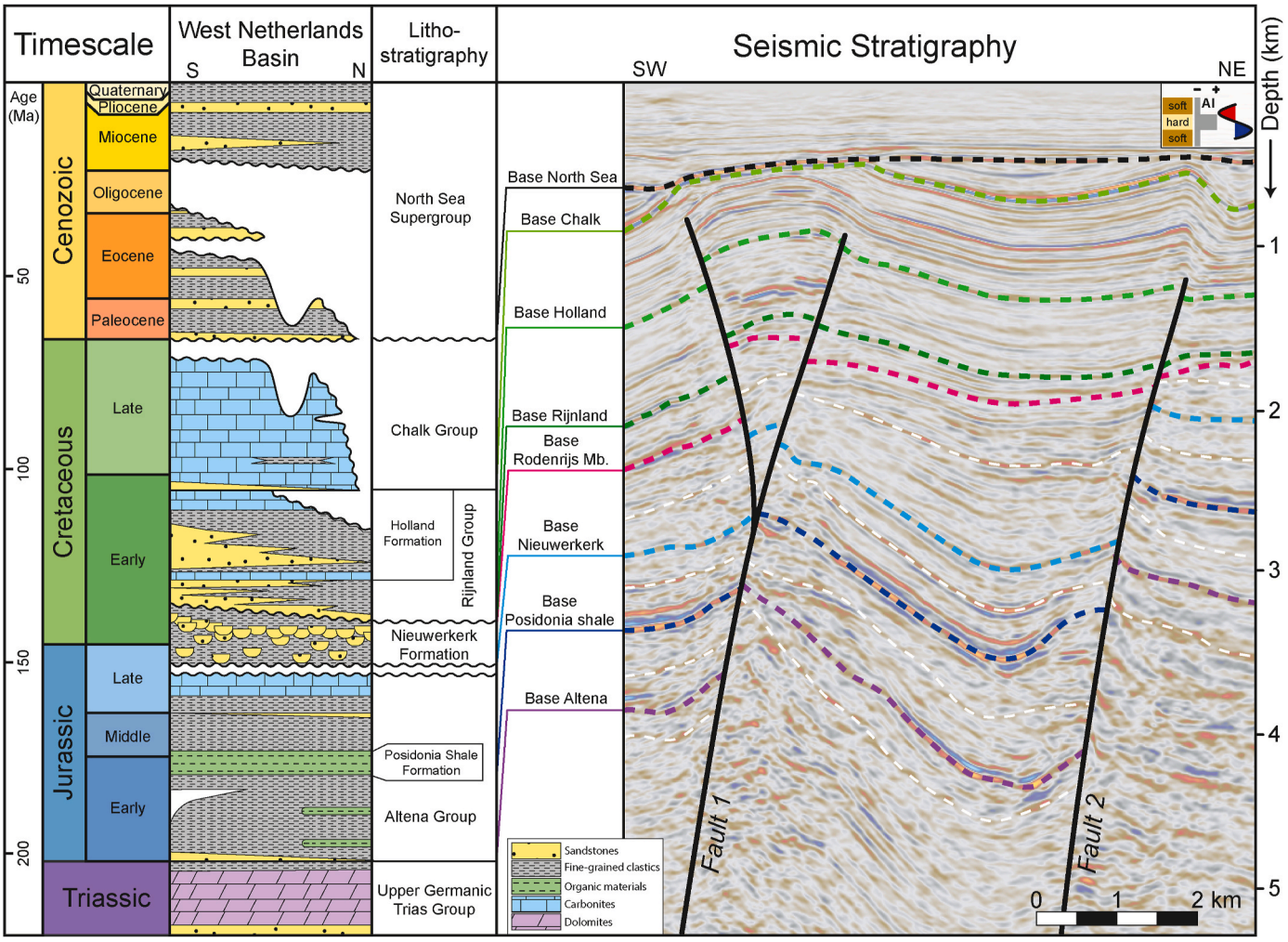

Fig. 3. Lithostratigraphic chart of the West Netherlands Basin, showing a simplified stratigraphy, a section of inline 3230, the interpreted horizons and their age, and studied faults 1 and 2. All horizons, except the black dotted line of the base North Sea Supergroup, were used for the construction of the displacement-distance diagrams. The white dotted horizons show the additional horizons used for the along-dip diagrams (Figs. 7 and 9). The seismic display also shows a pop-up structure in the SW, above Fault 1, and a gentle fault-propagation fold towards the NE, above Fault 2. This figure is based on Weert et al. (2024).

throw values were obtained from the along-strike diagrams and cross-checked in both Petrel and 3D Move. The horizons incorporated in the along-dip diagrams comprise the earlier mentioned bases of the Chalk, Rijnland and Altena groups and the Nieuwerkerk and Posidonia Shale formations. To increase the datapoint density, six additional horizons were interpreted in the proximity of the studied faults and analysed to obtain their fault throw value and their distance to the upper fault tip. For the faults that only experienced extension, the base of the Early Cretaceous Rodenrijs Claystone Member and four ad hoc mapped horizons in between the regionally mapped surfaces were added to the interpretation (pink and white dotted horizons, Fig. 3). For the faults that also experienced transpressional inversion, the base of the late Early Cretaceous Holland Formation was included as well (Fig. 3). The base of the Chalk Group was not included in the along-dip diagrams, as that surface is overlying the fault tips.

5. Results

In this section, the along-strike and along-dip displacement-distance diagrams (DDD) of the nine studied faults are described. Faults F3, F4, F5, and F9 are located in the southern part of the study area (Fig. 5), where transpressive inversion is negligible (these faults are hereafter called ‘extensional faults’). This is in agreement with the mapped surfaces for the base of the Rijnland and Chalk groups, which display negligible inversion-related deformation (i.e., folding) above these faults (Fig. 5a). Therefore, only the Jurassic sedimentary succession is included in their along-strike and along-dip diagrams. Conversely, faults F1, F2, F6, F7, and F8 experienced fault inversion (hereafter called ‘inverted faults’), wherefore the diagrams of these faults include both the Jurassic and Cretaceous sedimentary succession.

5.1. Extensional faults

Faults F3, F4, F5, and F9 generally strike NW-SE (Fig. 5). Specifically, the majority of F3, F5, and the northern part of F4 strike NNW-SSE. F9 and the southern sections of F3 and F4 strike NW-SE. The northwestern-most tip of F9 extends just outside the study area, while F3, F4, and F5 are fully included in the dataset. The Jurassic sedimentary succession in the dataset’s southern half shows non-deposition and erosion near the basin edge, leading to the absence of the Posidonia Shale Formation at the basin’s margins. Consequently, the dark blue layer is missing for parts of F3, F5, and F9, near the basin’s edge (Fig. 6).

The along-strike DDDs display fully connected and partly unconnected bell-shaped patterns. Partly unconnected displacement patterns feature overlapping or underlapping fault segments, yet, the resolution of the data is too low to discriminate between overlapping and underlapping features. Therefore, for the faults showcasing separate segments, the possible relationship is indicated by dashed lines in the along-strike

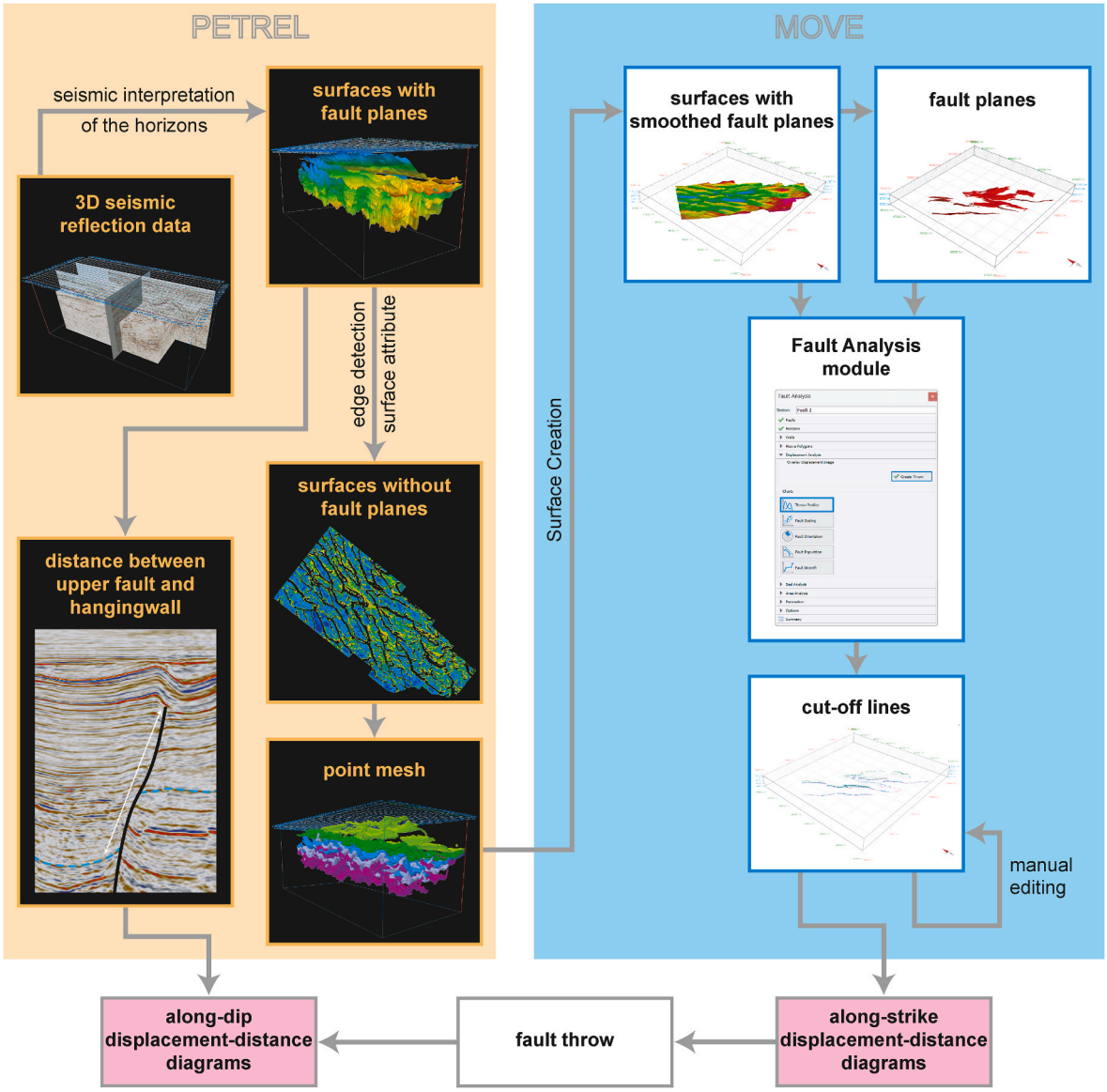

Fig. 4. Schematic chart showing all steps described in the methods section that were taken to produce the along-dip and along-strike displacement-distance diagrams.

DDDs.

5.1.1. Fault 3

The seismic depth maps of the Altena Group (Fig. 5c) and Nieuwerkerk Formation (Fig. 5b) show two segments for F3. On the along-strike DDDs, the two fault segments are indicated by two displacement maxima with a bell-shaped distribution, which is more pronounced for the Altena Group (purple horizon) than for the Nieuwerkerk Formation (light blue horizon). Since the Posidonia Shale Formation (dark blue horizon) is eroded towards the south, it is only present as a dark blue displacement maxima on the right side of the diagram. Possible linkage between the two maxima is indicated by the dashed lines in the purple and light blue horizons. Thus, we identified three key markers: two marking the lateral tips of F3 (T1 and T2) and one marking the displacement low or 'saddle' between the faults' segments (S1, Fig. 6). At T2, the three horizons are all superposed at the same lateral distance.

F3 is intersected by two along-dip DDDs, F3-1 and F3-2 (Figs. 6 and 7), both located in the right displacement maxima, as the dark blue horizon is eroded in the left maxima and layer correlation across the fault is elusive. Both diagrams consist of three displacement gradients, that are connected by kink points (KP) in displacement (KP1 and KP2 for F3-1, and KP3 and KP4 for F3-2) (Fig. 7). The displacement gradient in F3-1 is similar before and after KP1 and KP2, while in between both KPs it displays a decrease. In F3-2, the displacement gradient decreases upward (Fig. 7).

5.1.2. Fault 4

Between the fault tips of F4 (T3 and T4, Fig. 6), four connected displacement maxima are visible, linked by displacement lows (S2, S3, and S4, Fig. 6), which is consistent with the seismic depth maps, showing one continuous fault (Fig. 5b and c). The pattern is consistent across all three horizons, except for the dark blue horizon on the left side of the diagram, where it is eroded. Also here, at T4, the three horizons are all superposed at the same lateral distance. The difference in fault throw value between two horizons, or displacement ratio, is variable along the length of the fault. The along-dip DDD for F4 shows two trends in displacement gradients linked by KP5 for F4-1, and three trends divided by KP6 and KP7 for F4-2. Here, the fault gradient is similar before KP6 and after KP7, displaying a decrease between KP6 and KP7 (Fig. 7).

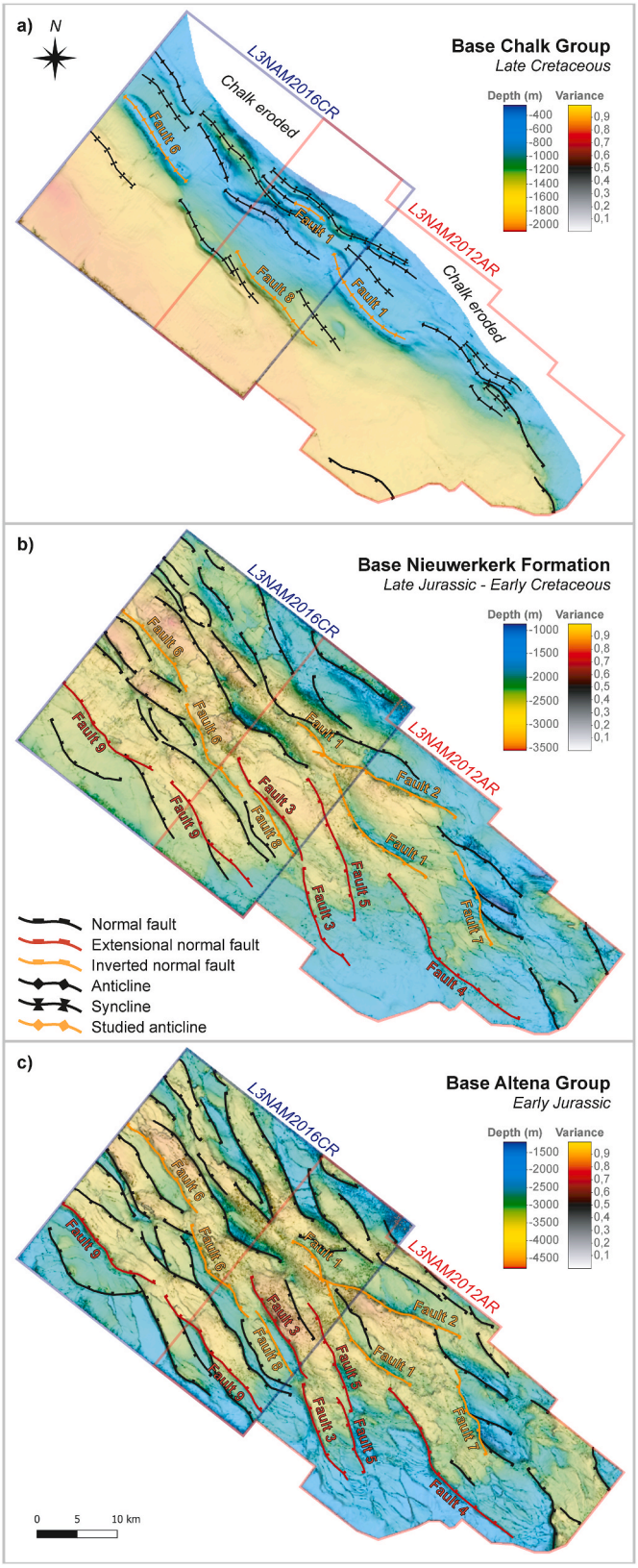

Fig. 5. Maps of: (a) the base Chalk Group, (b) the base Nieuwerkerk Formation, and (c) the base Altena Group. Each map is composed of the seismic depth map with an overlay of the variance attribute in 40% transparancy. The studied extensional faults are marked red and the inverted faults orange. The inversion structures that are linked to underlying studied faults are marked orange. (For interpretation of the references to colour in this figure legend, the reader is referred to the Web version of this article.)

5.1.3. Fault 5

The seismic depth maps display two fault segments for F5, with overlapping segments with a relay ramp at the depth of the Altena Group (Fig. 5c), and one continuous fault at the depth of the Nieuwerkerk Formation. Here, only the northern segment is reactivated, while the southern segment shows minor displacement (Fig. 5b). On the along-strike DDD, the fault is characterized by three displacement maxima between its fault tips (T5 and T6, Fig. 6). The northern segment contains a displacement low at marker S5 on all horizons. The low at S6 represents the possible linkage between the northern and southern segments, indicated by dashed lines for the dark blue and purple horizons. As the southern segments only show minor displacement at the level of the Nieuwerkerk Formation, its possible throw is indicated by a dashed line. Located between markers T5 and S5, along-dip DDD F5-1 and F5-2 show three trends in displacement gradients separated by KP8, KP9, KP10, and KP11 (Fig. 7). Here, the displacement gradient is similar before KP8 and KP10, and after KP9 and KP11, displaying a relatively high gradient. In between KP8 and KP9, and KP10 and KP11, the gradient shows a decrease. Located between S5 and S6, F5-3 displays a high displacement gradient before KP12, which decreases afterwards. F5-4 shows high displacement gradients before KP13 and between KP14 and KP15, and a decreasing gradient between KP13 and KP14, and after KP15 (Fig. 7).

5.1.4. Fault 9

F9 shows two fault segments at the depth of the Altena Group (Fig. 5c) and a single fault at the level of the Nieuwerkerk Formation (Fig. 5b). On the along-strike DDD, only the southeastern fault tip (T7) is visible, as its northwestern tip is located outside the study area. The pattern is characterized by three displacement maxima that are connected by two displacement lows (S7 and S8), with the low at S8 being present in all horizons (Fig. 6). The dark blue horizon displays only two maxima, as it is eroded towards the northwest. The minima at S7 represent the possible linkage of the two segments, interpreted by dashed lines. Here, the dark blue and purple horizons likely show no displacement and the light blue horizon a possible linkage. Along-dip DDD F9-1 is composed of three trends in fault gradients; a high displacement gradient before KP16 and after KP17, and a decreasing gradient between KP16 and KP17. F9-2 and F9-3 show four trends; a high gradient before KP18 and KP21, between KP19 and KP20, and between KP22 and KP23. Between KP18 and KP19, between KP21 and KP22, and after KP20 and KP23, a decrease in displacement gradient is observed (Fig. 7).

5.1.5. Summarizing faults 3, 4, 5, and 9

In summary, F3, F4, F5, and F9 show no evidence for transpressional inversion, and their DDDs display evidence of the accumulation of displacement during the two extensional events. The seismic depth maps show single faults (F4) and faults composed of two segments (F3, F5, and F9). These segmented faults are distinct at the depth of the Altena Group (Fig. 5c), with unclear possible linkage at the level of the Nieuwerkerk Formation, due to multiple small-scale faults (Fig. 5b). The along-strike DDDs feature displacement maxima that are approximately located close to the centre of the fault or fault segment, which are connected by displacement lows or ‘saddles’. Possible linkage between fault segments is indicated by dashed lines in the along-dip DDDs (e.g., F3, F5 and F9, Fig. 6). The displacement maxima of the patterns vary, with the purple horizon ranging from two to four times the size of the light blue, which is an indication for multi-phase rifting. F3 and F4 show superposed horizons at the same lateral distance at their fault tips (T2 and T4), indicating that the fault tips stayed fixed during the reactivation events. In the along-dip DDDs, three patterns are observed: displacement gradient trends that are either linked by one, two or three KPs. Generally, the DDDs show alternating high gradient and low gradient trends (Fig. 7). These high gradient trends generally appear at the level of the Nieuwerkerk Formation and lower part of the Altena Group, while the lower trends are observed around the depth of the Posidonia Shale Formation

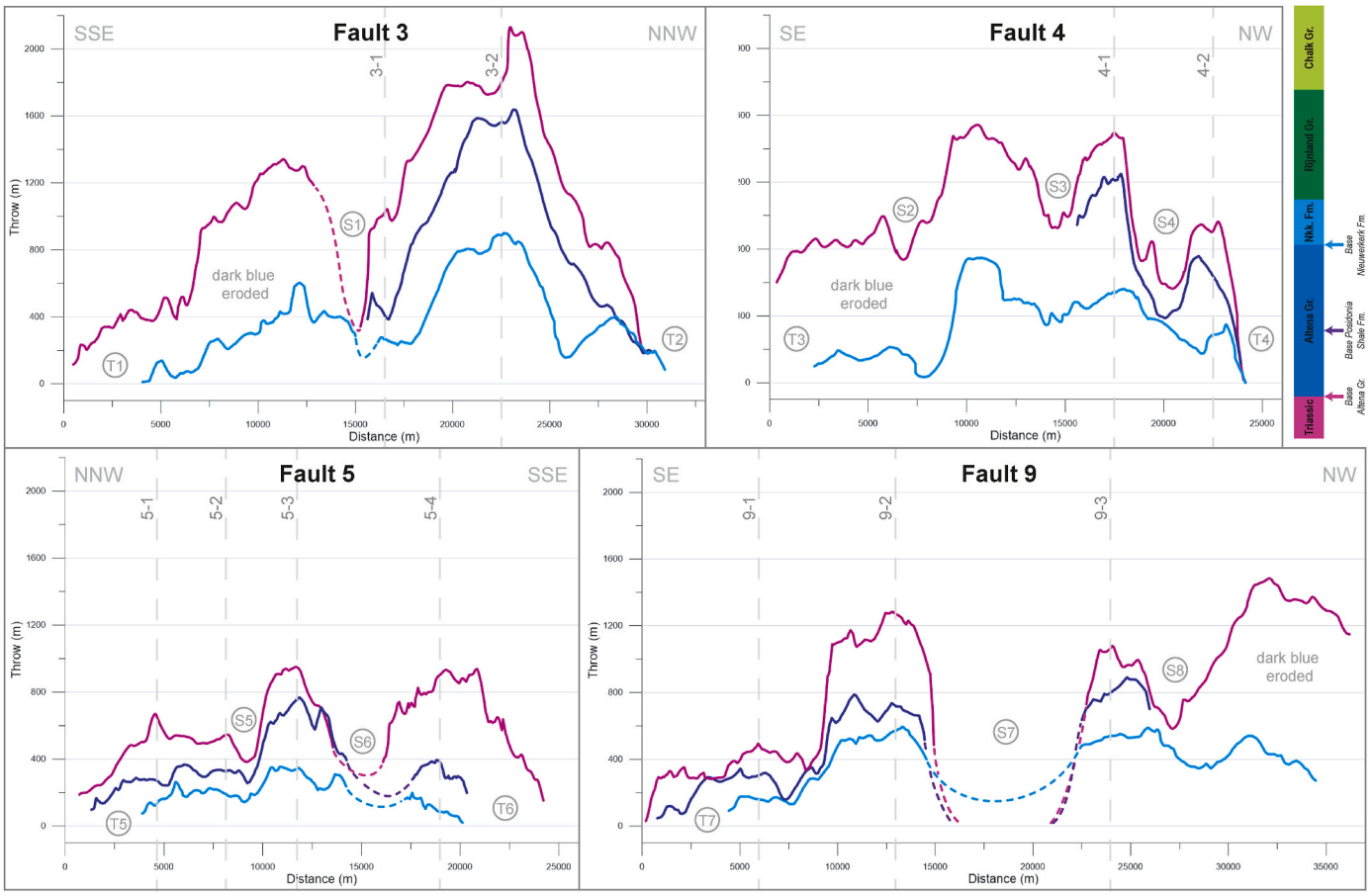

Fig. 6. Along-strike displacement-distance diagrams for F3, F4, F5 and F9. The profiles of the along-dip diagrams of Fig. 7 are indicated by the dashed lines. The markers with a T indicate fault tips, and the ones with an S saddles between fault throw maxima.

and below the Altena Group. Yet, the exact depths seem to vary from fault to fault. For example, F5-1 and F5-2 shows two trends with a high gradient separated by a low displacement gradient, F5-3 shows a gradient that is decreasing upwards, and F5-4 also shows two trends with a high gradient, intertwined by two trends with a low gradient. This corresponds with the along-strike DDD of F5, where the purple horizon displacement maxima is twice that of the light blue on the left side of the diagram (at F5-1 and F5-2), three times larger in the middle (at F5-3), and four times larger on the right side (at F5-4). This might suggest multiple phases of syn-sedimentary activity for F5-1, F5-2 and F5-4, separated by quieter periods.

5.2. *Inverted faults*

The faults that experienced positive, transpressive basin inversion, F1, F2, F6, F7 and F8, are located in the northern half of the dataset (Fig. 5). In the central part of the dataset, F7 and F8 strike NNW-SSE, and F1 and F6 strike NW-SE. Further towards the northeast, F2 strikes WNW-ESE. On its northwestern segment, F1 displays a sinistral displacement by F2 (Fig. 8). This strike slip displacement is most distinct at the depth of the Altena Group (Fig. 5c), but is also recognizable higher up in the stratigraphy (Fig. 5b). As the two segments of F1 have been displaced and were once continuous, both fault segments are treated as one fault. Erosion of the Chalk Group towards the northeast (Fig. 5a) means that the light green horizon is absent on the right side of the along-strike DDD of F2 (Fig. 8). The bases of the Rijnland and Chalk groups show non-deformation for parts of F2 and F6 (Fig. 5a), making the Rijnland Group missing in the eastern segment of F2 and the Chalk Group missing in the southern segment of F6 (Fig. 8).

The along-strike diagrams of F1, F2, F6, F7, and F8 feature both the Jurassic sequence (purple, dark, and light blue horizons) and the Cretaceous sequence (dark and light green horizons) (Fig. 8). The Cretaceous sequence was deposited after the basin's extensional phase, so before or during the inversion-related buttressing. Representing reversed motion, its throw values are negative. As the Jurassic sequence has undergone the same reversed motion, some fault tips display negative values. Examples are found in F1 (purple horizon at T0 and light blue horizon at S1) and F8 (dark blue horizon at T8 and T9, Fig. 8).

5.2.1. *Fault 1*

F1 is composed of two individual fault segments that are sinistrally displaced by F2 on seismic depth maps of the Altena Group and Nieuwerkerk Formation (Fig. 5b and c). At the top of the sequence, the Chalk Group shows folding, where the fold crest seems to increase in elevation away from the fault tips (Fig. 5a). The along-strike DDD of F1 is characterized by two separate fault segments, with two fault tips (T0 and T1) and a gap (S1, Fig. 8). S1 represents the location where F1 is displaced by F2. At both T0 and T1, superposed horizons for both sequences at the same lateral distance are observed. Both fault segments exhibit displacement maxima, with the maxima on the left fault segment having an approximately bell-shaped profile, while the maxima in the right fault segment has an approximately plateau-shaped profile. The maxima are observed both in the Jurassic and Cretaceous sequences, with the Jurassic showing higher throw values then the Cretaceous. The displacement ratio varies, particularly within the Jurassic sequence. Here, the dark blue horizon moves between the purple and light blue horizons. In the Cretaceous sequence, the light green horizon shows more displacement than the dark green between S1 and T1, and at T0. In

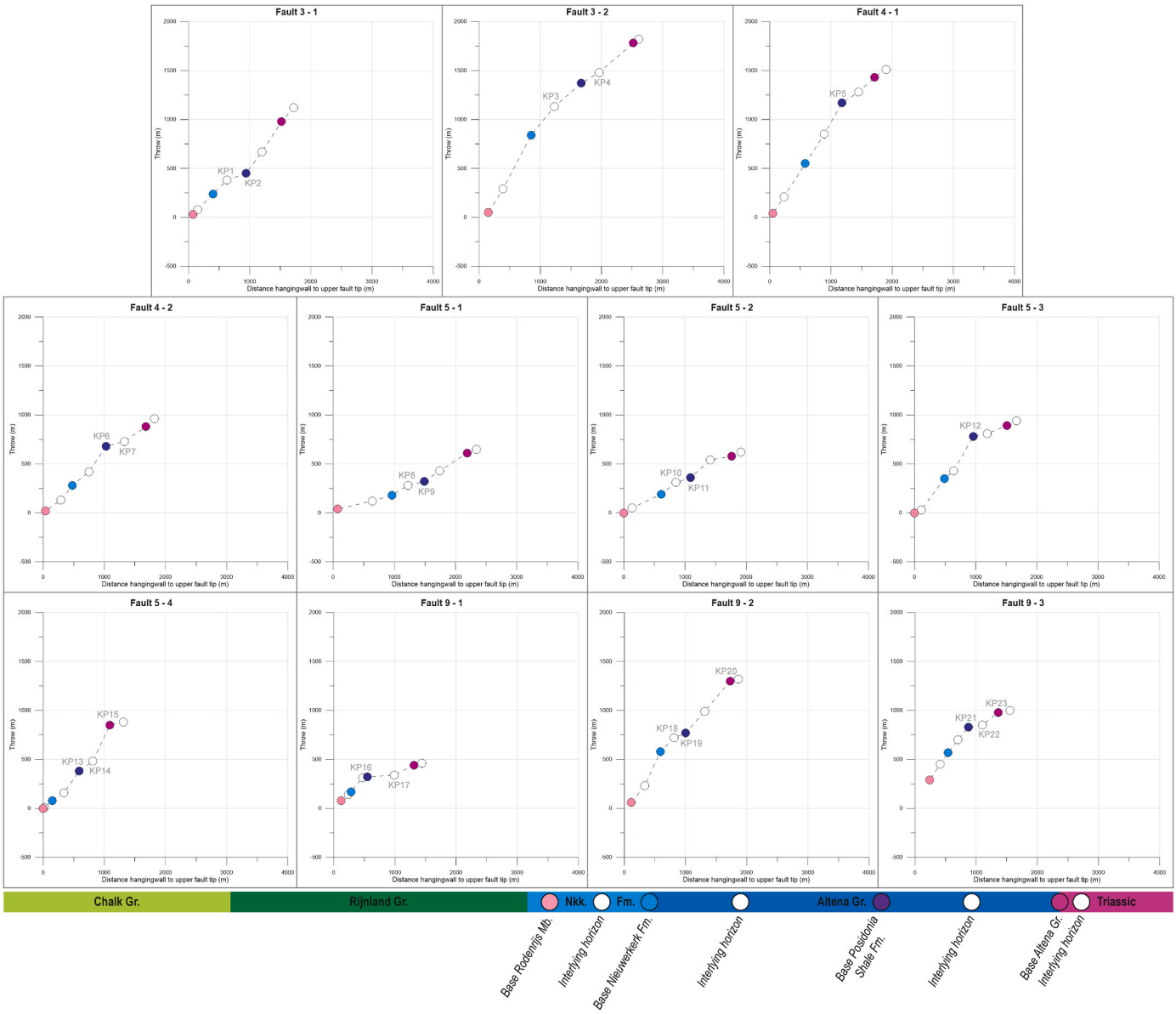

Fig. 7. Along-dip displacement-distance diagrams for F3, F4, F5 and F9. The kink points linking different linear trends are indicated by kink points (KP).

these areas, seismic data reveals a positive flower or pop-up structure (e.g., Fig. 3).

The along-dip DDDs of F1 reveal three to four KPs per profile. Each of the four diagrams show a consistent decreasing, negative displacement gradient for the Cretaceous sequence, which shifts to an increasing, upward trend after KP1, KP4, KP8, and KP12, all situated at the stratigraphic level of the base of the Rijnland Group. This increasing trend then transitions to a gentler curve after KP2, KP5, KP9, and KP13, at the depth of the Rodenrijs Member. Subsequently, in the Jurassic sequence, only F1-1 shows one KP with a displacement gradient that is decreasing upwards, while F1-2, F1-3, and F1-4 show two KPs, with alternating high gradient and low gradient trends (Fig. 9).

5.2.2. *Fault 2*

On the seismic depth maps of the Altena Group and Nieuwerkerk Formation, F2 is characterized as a single fault with a topographic low at the location where it displaces F1 (Fig. 5b and c). Above, the Chalk Group only shows significant folding in the faults' west northwestern domain, being eroded towards the east-southeast (Fig. 5a). On the along-strike DDD, the fault shows two displacement maxima connected by the mentioned displacement low (S2) between its fault tips (T2 and T3, Fig. 8). Superposed horizons at the same lateral distance are observed at both fault tips of F2. The maxima are more pronounced in the Jurassic sequence, with larger displacements compared to the Cretaceous horizons. Again, a varying displacement ratio is observed for the Jurassic sequence. Within the Cretaceous sequence, the dark green horizon forms two small displacement maxima, with their unconnected tips aligning with the Jurassic displacement low at S2. This suggests that F2 reactivated as two separate faults during the Cretaceous. On the left side of the diagram, the light green horizon plots within the left dark green horizon maxima, while on the right it is eroded. Here, the dark green pattern is absent due to non-deformation.

The along-dip DDD of F2-2 follows a similar pattern as the DDDs of F1, where the Cretaceous sequence first shows a decreasing negative trend that increases above KP20. In contrast, F2-1 and F2-3 show only a constant increasing trend in displacement gradient that becomes steeper after KP16 and KP24. For the Jurassic sequence, F2-2 and F2-3 show two trends with a constant high gradient that are interrupted by a low gradient trend. F2-1 shows a similar trend, but with an additional decreasing upward trend after KP19 (Fig. 9).

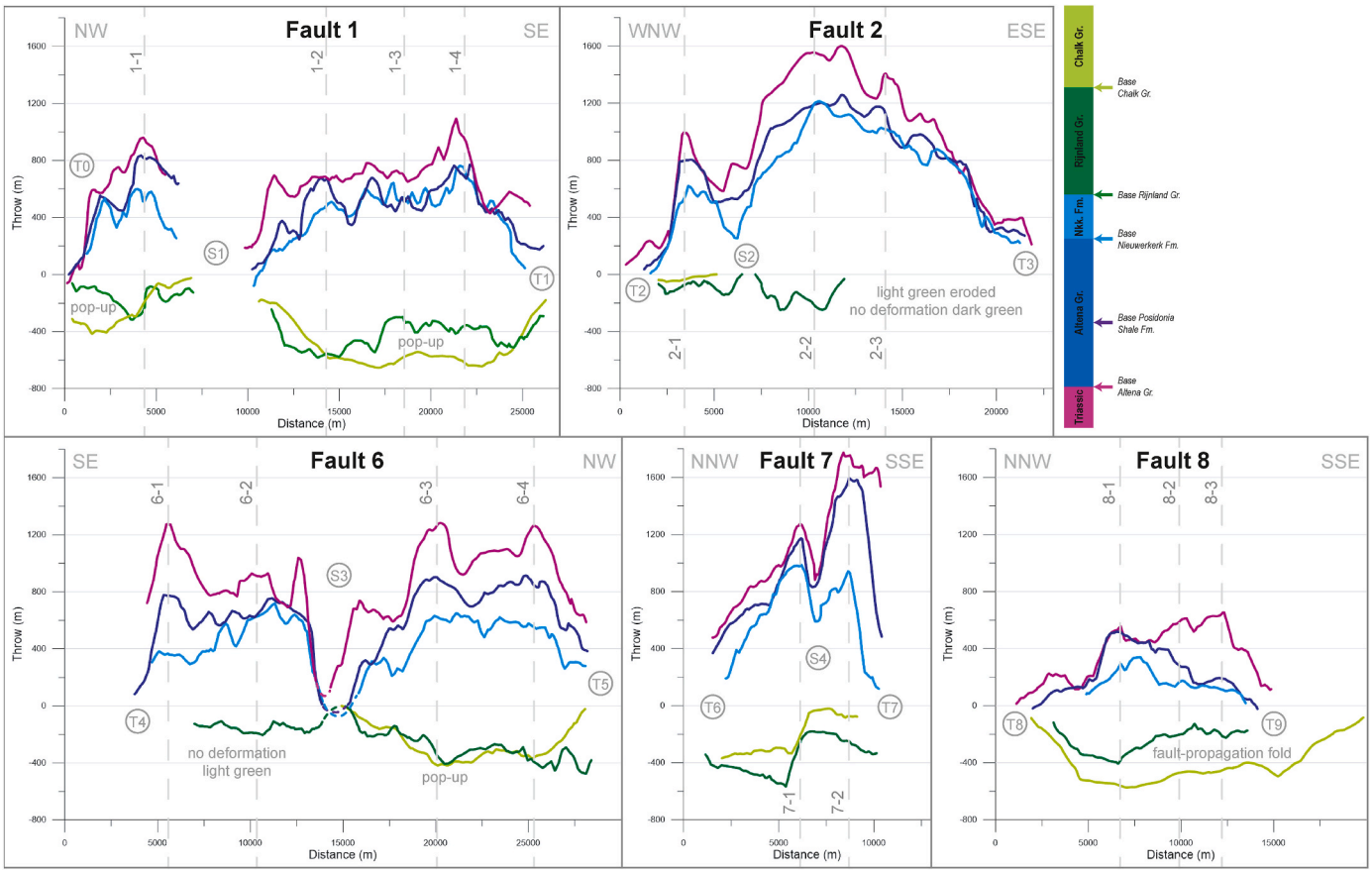

Fig. 8. Along-strike displacement-distance diagrams of F1, F2, F6, F7 and F8. The profiles of the along-dip diagrams of Fig. 9 are indicated by the dashed lines. The markers with a T indicate fault tips, and the ones with an S saddles between fault throw maxima.

5.2.3. *Fault 6*

The seismic depth maps of both the Altena Group and Nieuwerkerk Formation show two possibly linked fault segments for F6 (Fig. 5b and c). Only the northwestern fault segment displays folding for the Chalk Group (Fig. 5a). The along-strike DDD of F6 consists of two approximately plateau-shaped displacement maxima between its fault tips (T4 and T5), that are possibly linked by a displacement low (S3, Fig. 8). Again, superposed horizons at the same lateral distance are observed at the fault tips. Like F3, F5, and F9 (Fig. 6), the displacement low of F6 corresponds to an area with multiple small-scale faults (Fig. 5b and c), likely making the cumulative displacement non-zero, here indicated by dashed lines. Variations in the displacement ratio are observed in the Jurassic sequence. In the right bell of the Cretaceous sequence, the light green horizon displays more displacement compared to the dark green horizon. Similar to F1, seismic data reveals a pop-up structure here. On the left side of the diagram, the light green horizon shows no deformation and is therefore absent.

With the Cretaceous sequence being absent, the along-dip DDD for F6-1 resembles those of the extensional faults, with alternating high gradient and low gradient trends between KP27 and KP28, and after KP29 (Fig. 9). The other three diagrams are similar to those of F1 and F2-2, featuring a decreasing, negative trend for the Cretaceous sequence that turns into an increasing trend after KP30, KP34, and KP38. F6-2 and F6-3 then shows alternating high gradient and low gradient trends between KP32 and KP33, and KP36 and KP37. F6-4 shows a decreasing upward trend for the Jurassic sequence (Fig. 9).

5.2.4. *Fault 7*

F7 is characterized as one single fault on the seismic depth maps (Fig. 5). It is bordering two faults on its northeastern side (Fig. 5c) and shows folding (Fig. 5a). The along-strike DDD consists of two displacement maxima connected by a displacement low (S4) between its fault tips (T6 and T7, Fig. 8). The peaks of the maxima correspond to the locations where the neighbouring faults are bordered. While the maxima display similar patterns for both the Jurassic and Cretaceous sequences, variations in displacement ratio are observed. In the Jurassic sequence, the right maxima exhibits bigger displacement than the left, whereas in the Cretaceous sequence, this pattern is reversed with the left maxima showing bigger displacement. The along-dip DDDs of F7 (F7-1 and F7-2, Fig. 9) display a declining, negative trend in the Cretaceous sequence that shifts to a steep upward trend after KP41 and KP46. The displacement gradient then shows alternating high gradient and low gradient trends for the Jurassic sequence in both DDDs (Fig. 9).

5.2.5. *Fault 8*

F8 is located close to F3, being composed of a single fault (Fig. 5). It borders a stratigraphic high, clearly visible at the depth map of the Altena Group (Fig. 5c) and shows folding (Fig. 5a). Its along-dip DDD is characterized by a single displacement maxima (between T8 and T9, Fig. 8). At both T8 and T9, superposed horizons for both sequences at the same lateral distance are observed. Only for T9 the light green horizon extends beyond the fault tip. Seismic data indicates a significant fault-propagation fold above the fault tips, over the entire length of F8, stretching out towards the southeast. (e.g., Fig. 3, but with a higher elevation). Here, the light green horizon shows a higher displacement than the dark green horizon. Within the Jurassic sequence, displacement ratios vary as well, with the dark blue horizon shifting between the purple and light blue horizons. The along-dip DDDs of F8 reveal a similar trend for the Cretaceous sequence as seen in F1, F2-2, F6, and F7. Subsequently, all three diagrams show alternating high gradient and low

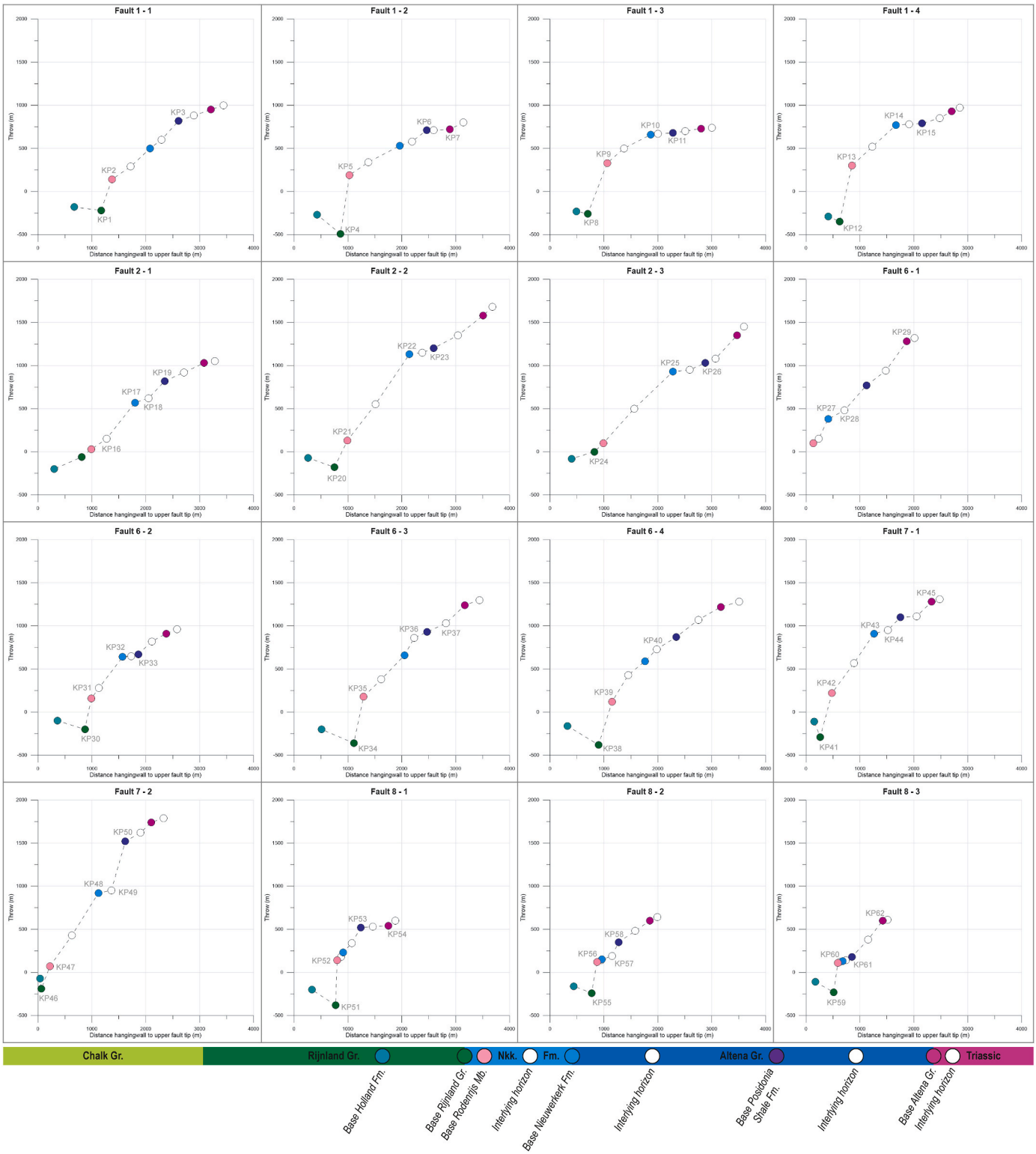

Fig. 9. Along-dip displacement-distance diagrams for F1, F2, F6, F7 and F8. The kink points linking different linear trends are indicated by kink points (KP).

gradient trends, scattered across the Jurassic stratigraphy (Fig. 9).

5.2.6. *Summarizing faults 1, 2, 6, 7, and 8*

Summarizing, F1, F2, F6, F7, and F8 show clear evidence for transpressive inversion. The seismic depth maps mainly show single faults at the depth of the Altena Group and Nieuwerkerk Formation, where only F6 is composed of two possibly linked segments (Fig. 5b and c). The depth map of the Chalk Group shows folding above the faults, in response to reversed reactivation (Fig. 5a). In the DDDs, inversion is characterized by negative throw values (i.e., reverse displacement) at the Jurassic fault tips and in the Cretaceous sequence. Interestingly, the tips of both the extensional and inverted horizons, i.e. the Jurassic and Cretaceous sequences respectively, show no lateral propagation, with the fault tip locations remaining fixed. Transpressive inversion-related structures, such as positive flowers and major fault-propagation folds, are recognized in the seismic data and the along-strike DDD, where they

are indicated by larger amplitudes for younger layers (e.g., F1, F6, and F8, Fig. 8). In the along-dip DDDs, the values of the positively inverted horizons plot below zero, showing an increasing trend towards the fault tips (Fig. 9).

The Jurassic sequence exhibits signs of multi-phase rifting. The along-dip DDDs show a similar behaviour as observed for the extensional faults: displacement gradients that show alternating trends with a consistent high displacement gradient and a decreasing gradient. Also, in the along-strike DDDs, multiple rifting events can be recognized by interpreting the varying displacement ratios between the different patterns. For example in F1, where the left displacement maxima in the along-strike DDD shows the purple horizon's displacement is a half time larger than that of the light blue, with F1-1 displaying only a decreasing upward trend for the displacement gradient of the Jurassic sequence. Going to the right displacement maxima, the purple horizon is up to twice the size of the light blue horizon. Here, F1-2, F1-3, and F1-4 show two trends of consistent high displacement gradients for the Jurassic sequence, indicating two syn-sedimentary phases of faulting separated by less active periods. These less active periods are illustrated by near-horizontal, or decreasing trends for the displacement gradient, for example between KP6 and KP7 in F1-2. In the along-strike DDD of F1, the purple and dark blue horizons show similar displacement at F1-2, where the along-dip DDD shows a near-horizontal trend. A similar trend is observed at F1-3 and F1-4, where the dark and light blue horizons show a similar displacement, with their along-dip DDD displaying a near-horizontal trend at these depths. Consequently, where the horizons have different displacements, such as at F1-1, no near-horizontal pattern is observed in the along-dip DDD. Thus, pre- and post-rift periods are likely identified by horizons with similar displacements in the along-strike DDDs and near-horizontal curves in the along-dip DDDs. Another example of pre- and post-rift periods can be observed on F8, which also illustrates that the periods of syn-kinematic sedimentation can vary along the length of a fault. On the left side of the along-strike DDD, syn-sedimentary activity is seen during the Late Jurassic and Triassic (F8-1), while on the right side (F8-3), the activity shifts to the Early Jurassic and Triassic.

5.3. Correlation diagrams

Different features are observed on the DDDs of the nine faults analysed. Specifically, the throw or displacement gradients in the along-dip DDDs show clear evidence of the activity of the faults during the rifting events. Faults active during both rifting events are characterized by a near-horizontal trend, or low displacement gradient, between two segments with a steep trend, or high displacement gradient. To explore potential correlations, the displacement gradients of the segments (that are divided by KPs) were measured. For example, in F2-2, a high displacement gradient of 54° is observed between KP21 and KP22, followed by low gradient with an angle of 13° between KP22 and KP23, and a high gradient of 34° from KP23 onwards (Fig. 9).

When plotting the displacement gradients in a histogram, a clear division is observed (Fig. 10a). The tectonic quiescent periods, interpreted as pre- and post-rift periods, show gradients between 0° and 40°. The majority of the fault segments active during rifting show gradients between 30° and 60°, with the Early Jurassic rift event showing a peak between 30° and 50°, and the Late Jurassic rift event peaks between 45° and 60°. The gradients for the inverted fault segments, measured between the bases of the Rijnland Group and Rodenrijs Claystone Member, show values between 60° and 90°. The diagram shows that fault segments with the lowest amount of reactivation typically have the lowest displacement gradients, followed by segments that experienced a single rift event, those that underwent two rifting events, and finally, segments that also experienced reversed reactivation, exhibiting the highest gradients. This might suggest that each event of fault reactivation increases the displacement gradient.

To explore the possibility of a correlation between the rifting events, the displacement gradients for the Early and Late Jurassic rifting events were plotted against each other (Fig. 10b). The majority of the faults

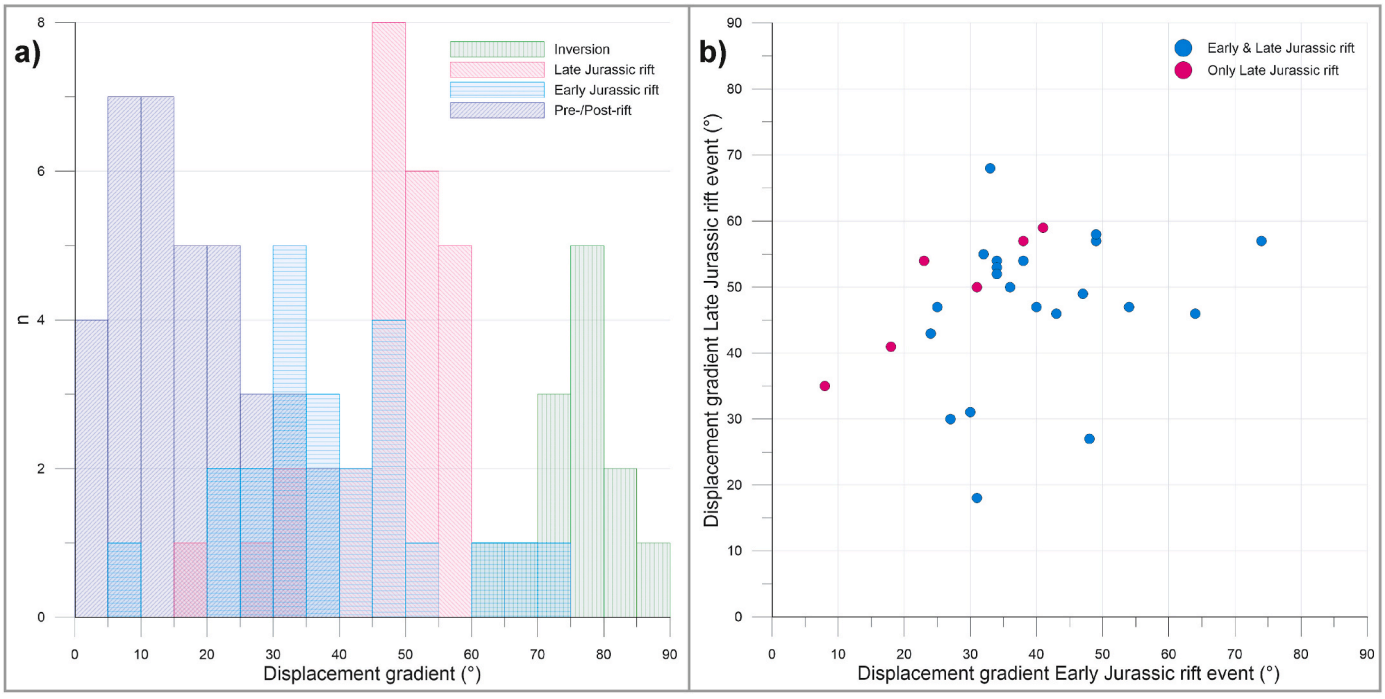

Fig. 10. Plots of the displacement gradient; (a): a histogram showing the displacement gradient of the different tectonic phases: quiescent periods (pre-/post-rift), syn-rift events (Early and Late Jurassic rifting), and basin inversion; (b): the displacement gradients of the Early Jurassic rift event plotted against those of the Late Jurassic rift event. The blue data points experienced both Early and Late Jurassic rifting, thus giving two clear displacement gradients. The pink data points only experienced the Late Jurassic rift, wherefore the displacement gradient for the Early Jurassic rift was measured between the base Posidonia Shale Formation and base Altena Group. (For interpretation of the references to colour in this figure legend, the reader is referred to the Web version of this article.)

experienced both rifting events (blue dots), but for the ones that only experienced the Late Jurassic rift event (pink dots), the displacement gradient for the Early Jurassic rift was measured between the base Posidonia Shale Formation and base Altena Group. The diagram clearly demonstrates that there is no correlation between the gradients from both events. This suggests that the growth mode, particularly the up-dip propagation of the fault tip, is not sensitive to fault inheritance from the first event.

6. Discussion

A detailed analysis of the displacement-distance diagrams (DDDs) for nine basin-scale faults in the West Netherlands Basin (WNB) showcases the complex interplay of Jurassic multi-phase rifting and Cretaceous basin inversion on fault evolution. The faults in the southern half of the dataset (F3, F4, F5, and F9) experienced at least two extensional events, showing different modes of fault propagation. Additionally, the faults in the northern half (F1, F2, F6, F7, and F8) show signs of transpressive inversion, evidenced by the presence of pop-up structures and fault-propagation folds.

6.1. Fault evolution

The along-strike DDDs indicate variations in displacement along the faults, showing displacement maxima separated by displacement lows or 'saddles' (Figs. 6 and 8). With the maxima representing fault segments and the lows indicating fault linkage, two general patterns are observed; patterns where all maxima and lows are connected (F1, F2, F4, F7, and F8), and unconnected fault segments (F3, F5, F6, and F9). Generally, the resolution of the seismic depth maps is not sufficient to distinguish between overlapping and underlapping fault segments. The exception is F5, which displays a relay zone at the depth of the Altena Group (Fig. 5c). The architecture of possible linkage remains unclear, especially at the level of the Nieuwerkerk Formation, mainly due to the presence of multiple small-scale faults (Fig. 5b and c).

After initiation, the faults in this study propagated upward rather than laterally throughout their life. This is indicated by the superposed fault tip locations up through the faulted succession, as indicated in the along-strike DDDs (e.g., F1, F2, F3, F4, F6, and F8). Here, the tips of the fault all plot at the same distance, including the layers that underwent transpressive inversion. Over time, the faults had fixed lateral tips, not propagating laterally, both during extension and inversion, which resulted in primarily sub-vertical, lateral tip-lines with an upward-moving upper tip line. This suggests rapid fault length development early in their history, with later reactivation events only increasing the faults' throw along the fault plane (Walsh et al., 2002; Childs et al., 2017). Therefore are the faults in this study most aligning with the constant-length coherent model (Walsh et al., 2002; Childs et al., 2017; Nicol et al., 2020), which is generally used to interpret the growth of individual faults during a single extension event. Interestingly, the faults in this dataset show that even during multiple extensional reactivation events and an inversion event, the lateral tips of the faults remain fixed and do not propagate laterally.

The fault growth interpretation for the faults in the WNB is further supported by two distinct along-strike DDD patterns. First there are approximately bell-shaped displacement maxima, indicating lateral fault growth in areas without pre-existing faults. Examples are F3, F4, and at the locations of F1-1 and F5-3, where the DDDs reflect only the effect of the Late Jurassic rifting event. Secondly, there are approximately plateau-shaped displacement maxima, reflecting rapid initial fault propagation, followed by displacement accumulation. These patterns occur where older faults accommodate faster propagation, as observed at F1-2, F1-3, F1-4, F5-1, F5-2, F6-1, and F6-2, where the DDDs show the influence of both the Early and Late Jurassic rifting events.

6.2. Multi-phase rifting

Multi-phase rifting is indicated by combining observations from the along-strike and along-dip DDDs. The along-dip DDDs illustrate the faults' vertical displacement profile, where kink points (KPs) mark different trends in displacement gradient, which indicate changes in the rate of displacement accumulation on the fault movement. A consistently high displacement gradient, or steep trend, in these diagrams indicates a rifting phase, while near-horizontal trends, or decreasing displacement gradients, suggest tectonically less active periods. For the Jurassic succession, three general patterns are observed in the along-dip DDDs: (1) decreasing upward trends with only one KP and no alternating near-horizontal trends, indicating one rifting event (e.g., F1-1, F4-1, and F5-3, Fig. 11a); (2) diagrams with two trends of a consistent high displacement gradient that are intertwined by a decreasing trend that is marked by two KPs, indicating two separate rifting events (e.g., F2-2, F6-2, and F9-1, Fig. 11b and c); and (3) diagrams with more than two KPs, where trends of consistent high displacement gradients and by near-horizontal trends alternate, indicating at least two rifting phases and more than one less active period (e.g., F5-4, F7-2, and F9-3, Fig. 11d). In the along-strike DDDs, the previously mentioned approximately bell or plateau shapes of the lateral displacement pattern can indicate rifting as well (Fig. 11). Generally, bell-shaped displacement maxima are observed for fault segments that only experienced one rift event, while the plateau-shaped displacement maxima are observed for some of the faults that underwent multiple rifting events. For these reactivated faults, a viable explanation is a mechanism of rapid fault surface propagation in the upper part of the sequence, while maintaining the lateral fault tips approximately fixed. Additionally, tectonically less active periods are clearly reflected by overlapping horizons. For instance, in F8, at location F8-1, the purple and dark blue horizons display a similar displacement, corresponding to a near-horizontal curve in the along-dip DDD. The same accounts for location F8-3, where a similar displacement is observed for the dark and light blue horizons (Fig. 8).

F8 also illustrates that various extensional events can occur along the length of a single fault. Notably, the timing of the tectonic quiet period changes from the Early Jurassic at F8-1 to the Late Jurassic for F8-3 (Figs. 8 and 9). Additionally, two rifting events can be observed in the along-dip DDD of F8-1 (between KP52 and KP53, and after KP54), while only one is observed for F8-3 (between KP61 and KP62, Fig. 9). Similar observations are made in F1, F3, F4, F5 and F6 (Figs. 7 and 9). By integrating the lateral DDDs with the seismic depth maps, it becomes evident that fault segments that only record the Late Jurassic rifting event are consistently oriented NNW-SSE. Yet, fault segments that recorded both the Late Triassic to Early Jurassic and Late Jurassic rifting phases strike both NNW-SSE and NW-SE. As a result, a single fault with internal bending can contain different segments that have undergone one and multiple reactivation events. This is in line with the concept that the underlying structural framework can modulate the segmentation of normal faults (Laó-Dávila et al., 2015; Manatschal et al., 2015; Brune et al., 2023). In the WNB, the Late Triassic to Early Jurassic rift phase developed upon the pre-existing NW-SE oriented structural framework, forming NW-SE-oriented faults. The subsequence Late Jurassic rift likely inherited the pre-existing NW-SE-oriented faults, which were more prone to failure and tended to localize deformation (e.g., Henza et al., 2010, 2011; Withjack et al., 2017; Zwaan and Scheurs, 2017; Wang et al., 2021; Zwaan et al., 2021; Osagiede et al., 2021; Kolawole et al., 2021; Bonini et al., 2023; Brune et al., 2023). As the extensional stress field rotated from NE-SW to ENE-WSW by the Late Jurassic (Weert et al., 2024), additional NNW-SSE striking faults were formed.

The alternating depths for the various events in the along-dip DDDs illustrate that rifting in the WNB was a continuous process, with culminations in the Early and Late Jurassic. Generally, there is a period of tectonic quiescence, a post-rift phase, around the depth of the Posidonia Shale Formation. Yet, the depth of the corresponding sub-horizontal trend in displacement gradient varies between the base of the

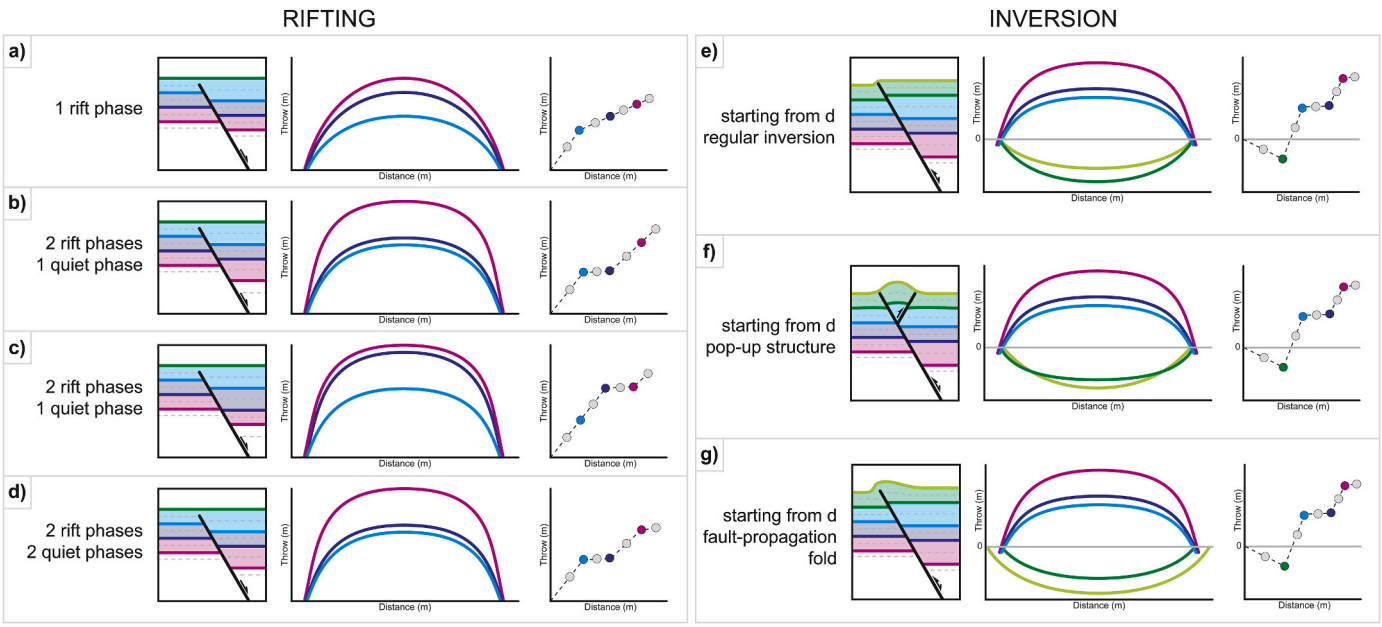

Fig. 11. Summarizing figure, showing all possible endmembers of the lateral and vertical displacement-distance diagrams. For each endmember a 2D representation of the fault and its associated lateral and vertical displacement-distance diagrams are shown. The extensional fault modes are displayed in; (a): with one rift phase and its associated bell-shaped lateral displacement pattern, (b and c): with two rift phases and one quiescent period, and (d): with two rift phases and two quiescent periods. The lateral patterns of b, c, and d show the characteristic plateau-shaped bells, associated with multiple phases of extension. For the inverted faults, endmember d is used as starting point; (e) inversion with displacement, but minor inversion structures, (f) with the development of a positive flower or pop-up structure, and (g): with the development of a large-scale fault-propagation fold.

Nieuwerkerk Formation (e.g., F2-2 and F6-2) and base of the Altena Group (e.g., F1-2 and F8-1). Furthermore, some along-dip DDDs show another quiescent period, likely a pre- or post-rift phase, below the Altena Group (e.g., F5-4 and F9-2), while others record rifting at this time (e.g., F1-4 and F3-1). This shows that the rotation of the tectonic stress field in the Jurassic was a gradual process.

6.3. Basin inversion

Reversed fault reactivation is characterized by negative values in the DDDs (Figs. 1, 8 and 9e, f, and g). In the Jurassic sequence, reversed reactivation caused negative values at the fault tips in the along-strike DDDs (at T0, S1, T8 and T9 in Fig. 8 and illustrated in Fig. 11e). Pop-up and significant fault-propagation folds are identified in the Cretaceous sequence. In these areas, the younger pattern of the Chalk Group shows a bigger displacement than the older Rijnland Group. While pop-up structures only tend to show this pattern in the middle segments of the faults (e.g., F1 and F6 in Fig. 8 and illustrated in Fig. 11f), fault-propagation folds cause this pattern to be present over the total length of a fault (e.g., F8 in Fig. 8 and illustrated in Fig. 11g). Here, the fold affects an area longer than that of the underlying fault, as evidenced by the longer displacement pattern of the Chalk Group.

Transpressive inversion gives a distinct negative trend for the displacement gradient in the along-dip DDDs (Fig. 11e, f, and g). Starting at the upper fault tip, represented by zero, then decreasing into negative values, due to compressional tectonics. A general turning point, where the decreasing displacement gradient becomes increasing, can be found around the depth of the base of the Rijnland Group. This turning point is interpreted to mark the change from net compression to net extension. Interestingly, F2-1 and F2-3 do not show this turning point for the measured depths in the Cretaceous sequence. Likely, it is recorded higher up in the stratigraphy, caused by a weaker effect of inversion on F2.

Transpressive inversion is more pronounced in faults striking NNW-SSE and NW-SE, characterized by higher throw values and the presence of pop-ups and fault-propagation folds (e.g., F1, F6, F7, and F8). In contrast, F2, which strikes WNW-ESE, shows less distinct effects of inversion. For F2, this can be attributed to the steep dip of 75° and the faults' strike-slip component, making it more difficult to invert (Lowell, 1995; Bonini et al., 2012; Zwaan et al., 2022 and references therein). While this may explain F2, it does not fully account for the basin's trend. Indeed, most transpressive inversion structures are NNW-SSE and NW-SE elongated, but WNW-ESE striking structures also appear in the depth map of the Chalk Group (Fig. 5a). The occurrence of these structures can be attributed to the angle between the shortening direction and elongation of the pre-existing faults (Lowell, 1995; Bonini et al., 2012; Zwaan et al., 2022 and references therein). The shortening direction during the Late Cretaceous is presumed to be SSE-NNW (Kley and Voigt, 2008), which is perpendicular to the WNW-ESE elongated faults, and subparallel to the NNW-SSE and NW-SE striking faults. Lowell (1995) suggested that faults with a 90° angle between their strike and the shortening direction, have a less favourable azimuth for fault reactivation than faults with an angle between 45° and 70°. This is due to the transpressional nature of basin inversion, where a 90° angle can cause the fault to 'lock'. In the WNB, the presence of inversion-related structures suggests a stronger compressional component over strike-slip, allowing minor inversion on high-angle faults. This also explains why later inversion was less strong in the WNB. The shortening direction changed to N-S during the Paleocene (Vandycke, 2002), lowering the angle for the majority of the faults, making them less prone to reactivation. Around early Miocene times, the stress field rotated to attain a NW-SE direction (Dèzes et al., 2004; Bourgeois et al., 2007), which is parallel to the basins' elongation, thus accommodating the tectonic stability up till today.

Apart from the mechanisms driving transpressive inversion, the architecture of the underlying extensional system also plays an important role (e.g., Cooper and Warren, 2020; Richetti et al., 2023; Vasey et al., 2024). When removing the bulk effect of inversion by flattening for the base Cretaceous in Petrel, it appears that the majority of the inversion-related structures are located on top of Triassic structural highs. Here, fewer Jurassic syn-kinematic sediments are present, making these areas weaker zones in the basin that are more prone to inversion

(e.g., Ziegler, 1989; Pinto et al., 2010; Richetti et al., 2023; Cooper and Warren, 2020).

7. Conclusions

Lateral (along-strike) and vertical (along-dip) displacement-distance diagrams produced for nine basin-scale faults in the WNB highlight key features for fault growth and displacement accrual in poly-phase settings.

Vertical displacement-distance diagrams reflect displacement gradients over time. High gradients indicate rifting phases, while low gradients mark pre- and post-rift periods. Transpressive basin inversion shows negative displacement gradients, that decrease from the fault tip to a turning point, whereafter the gradient increases. This turning point marks the change from net-compression to net-extension.

Lateral displacement-distance diagrams highlight throw patterns that distinguish tectonic phases. They indicate that faults reached their lateral lengths early in their growth history, with later reactivation only determining upward propagation of the fault plane while accumulating displacement. This is suggested by fixed fault tips, and the shape of the displacement maxima. Approximately bell-shaped displacement maxima were formed during initial lateral growth and are observed in faults active during a single rifting event. The bell-shaped maxima evolved into plateau-shaped displacement maxima after multiple phases of extensional activity. Basin inversion is marked by negative throw values. Here, younger horizons displaying higher displacement maxima than older ones indicate the presence of transpressional inversion-related structures, such as pop-ups and fault-propagation folds. Folds are evident, with longer lateral displacement in the folded horizons than in the faulted horizons.

This study demonstrates the value of displacement-distance diagrams for analysing fault growth and tectonic processes in complex geological settings, such as inverted rift basins. The proposed workflow and interpretation guide can be broadly applied to study the evolution of normal faults in similar geological settings worldwide.

CRediT authorship contribution statement

Annelotte Weert: Writing – original draft, Visualization, Methodology, Formal analysis, Data curation, Conceptualization. **Giovanni Camanni:** Writing – original draft, Conceptualization. **Marco Mercuri:** Writing – original draft, Methodology. **Kei Ogata:** Writing – original draft. **Francesco Vinci:** Writing – original draft. **Stefano Tavani:** Writing – original draft, Visualization, Methodology, Conceptualization.

Declaration of competing interest

The authors declare that they have no known competing financial interests or personal relationships that could have appeared to influence the work reported in this paper.

Acknowledgements

Daniele Blancone and Augusto Maresca are thanked for helping improve the workflow in Move. PanTerra Geoconsultants B.V. are thanked for funding the project. We thank DiSTAR of the University of Naples 'Federico II' for providing access to Schlumberger's Petrel Software (version 2020.3) and Petroleum Experts MOVE suite (version 2017.2). Finally, we thank the editor (Fabrizio Agosta), one anonymous reviewer, and Andy Nicol for their detailed and constructive comments and suggestions, which allowed us to improve the quality of the work.

All data used for this publication are open access and can be found on NLOG: https://www.nlog.nl/datacenter/smc-3d-surveys (last accessed on February 5, 2024). An overview of all Dutch seismic and well data in map view can be found here: https://www.thermogis.nl/mapviewer.

Data availability

All data is open access, the links are provided in the Acknowledgements

References

Agosta, F., Aydin, A., 2006. Architecture and deformation mechanism of a basin-bounding normal fault in Mesozoic platform carbonates, central Italy. J. Struct. Geol. 28 (8), 1445–1467. https://doi.org/10.1016/j.jsg.2006.04.006.

Alghuraybi, A., Bell, R., Jackson, C., 2023. A snapshot of the earliest stages of normal fault growth. τεκτονικα 1, 11–31. https://doi.org/10.55575/tektonika2023.1.2.29.

Barnett, J.A., Mortimer, J., Rippon, J.H., Walsh, J.J., Watterson, J., 1987. Displacement geometry in the volume containing a single normal fault. AAPG Bull. 71 (8), 925–937.

Bonini, L., Fracassi, U., Bertone, N., Maesano, F.E., Valensise, G., Basili, R., 2023. How do inherited dip-slip faults affect the development of new extensional faults? Insights from wet clay analog models. J. Struct. Geol. 169, 104836. https://doi.org/10.1016/j.jsg.2023.104836.

Bonini, M., Sani, F., Antonielli, B., 2012. Basin inversion and contractional reactivation of inherited normal faults: a review based on previous and new experimental models. Tectonophysics 522, 55–88. https://doi.org/10.1016/j.tecto.2011.11.014.

Bourgeois, O., Ford, M., Diraison, M., Veslud, C.L.C.D., Gerbault, M., Pik, R., Ruby, N., Bonnet, S., 2007. Separation of rifting and lithospheric folding signatures in the NW-Alpine foreland. Int. J. Earth Sci. 96, 1003–1031. https://doi.org/10.1007/s00531-007-0202-2.

Brune, S., Kolawole, F., Olive, J.A., Stamps, D.S., Buck, W.R., Buiter, S.J.H., Furman, T., Shillington, D.J., 2023. Geodynamics of continental rift initiation and evolution. Nat. Rev. Earth Environ. 4 (4), 235–253. https://doi.org/10.1038/s43017-023-00391-3.

Camanni, G., Childs, C., Delogkos, E., Roche, V., Manzocchi, T., Walsh, J., 2023a. The role of antithetic faults in transferring displacement across contractional relay zones on normal faults. J. Struct. Geol. 168, 104827. https://doi.org/10.1016/j.jsg.2023.104827.

Camanni, G., Freda, G., Delogkos, E., Nicol, A., Childs, C., 2023b. 3D geometry and displacement transfer of an oblique relay zone on outcropping normal faults. J. Struct. Geol. 177, 105001. https://doi.org/10.1016/j.jsg.2023.105001.

Childs, C., Watterson, J., Walsh, J.J., 1995. Fault overlap zones within developing normal fault systems. J. Geol. Soc. 152 (3), 535–549. https://doi.org/10.1144/gsjgs.152.3.0535.

Childs, C., Holdsworth, R.E., Jackson, C.A.L., Manzocchi, T., Walsh, J.J., Yielding, G., 2017. Introduction to the geometry and growth of normal faults. Geological Society, London, Special Publications 439 (1), 1–9. https://doi.org/10.1144/SP439.24.

Cooper, M., Warren, M.J., 2020. Inverted fault systems and inversion tectonic settings. In: Scarselli, N., Adam, J., Chiarella, D., Roberts, D.G., Bally, A.W. (Eds.), Regional Geology and Tectonics. Elsevier B.V., pp. 169–204. https://doi.org/10.1016/B978-0-444-64134-2.00009-2

Daniilidis, A., Doddema, L., Herber, R., 2016. Risk assessment of the Groningen geothermal potential: from seismic to reservoir uncertainty using a discrete parameter analysis. Geothermics 64, 271–288. https://doi.org/10.1016/j.geothermics.2016.06.014.

Delogkos, E., Manzocchi, T., Childs, C., Sachanidis, C., Barbas, T., Schöpfer, M.P., Chatzipetros, A., Pavlides, S., Walsh, J.J., 2017. Throw partitioning across normal fault zones in the Ptolemais Basin, Greece. Geological Society, London, Special Publications 439 (1), 333–353. https://doi.org/10.1144/SP439.19.

Delogkos, E., Manzocchi, T., Childs, C., Camanni, G., Roche, V., 2020. The 3D structure of a normal fault from multiple outcrop observations. J. Struct. Geol. 136, 104009. https://doi.org/10.1016/j.jsg.2020.104009.

Deng, C., Fossen, H., Gawthorpe, R.L., Rotevatn, A., Jackson, C.A., FazliKhani, H., 2017. Influence of fault reactivation during multiphase rifting: the Oseberg area, northern North Sea rift. Mar. Petrol. Geol. 86, 1252–1272. https://doi.org/10.1016/j.marpetgeo.2017.07.025.

Deng, H., McClay, K., Bilal, A., 2020. 3D structure and evolution of an extensional fault network of the eastern Dampier Sub-basin, North West Shelf of Australia. J. Struct. Geol. 132, 103972. https://doi.org/10.1016/j.jsg.2019.103972.

Dèzes, P., Schmid, S.M., Ziegler, P.A., 2004. Evolution of the European cenozoic rift system: interaction of the alpine and pyrenean orogens with their foreland lithosphere. Tectonophysics 389 (1–2), 1–33. https://doi.org/10.1016/j.tecto.2004.06.011.

Duffy, O.B., Bell, R.E., Jackson, C.A.L., Gawthorpe, R.L., Whipp, P.S., 2015. Fault growth and interactions in a multiphase rift fault network: horda Platform, Norwegian North Sea. J. Struct. Geol. 80, 99–119. https://doi.org/10.1016/j.jsg.2015.08.015.

Giba, M., Walsh, J.J., Nicol, A., 2012. Segmentation and growth of an obliquely reactivated normal fault. J. Struct. Geol. 39, 253–267. https://doi.org/10.1016/j.jsg.2012.01.004.

Hedlund, C.A., 1997. Fault-propagation, ductile strain, and displacement-distance relationships. J. Struct. Geol. 19 (3–4), 249–256. https://doi.org/10.1016/S0191-8141(96)00091-0.

Henza, A.A., Withjack, M.O., Schlische, R.W., 2010. Normal-fault development during two phases of non-coaxial extension: an experimental study. J. Struct. Geol. 32 (11), 1656–1667. https://doi.org/10.1016/j.jsg.2009.07.007.

Henza, A.A., Withjack, M.O., Schlische, R.W., 2011. How do the properties of a pre-existing normal-fault population influence fault development during a subsequent phase of extension? J. Struct. Geol. 33 (9), 1312–1324. https://doi.org/10.1016/j.jsg.2011.06.010.

Hughes, A.N., Shaw, J.H., 2014. Fault displacement-distance relationships as indicators of contractional fault-related folding style. AAPG Bull. 98 (2), 227–251. https://doi.org/10.1306/05311312006.

Jackson, C.A.L., Bell, R.E., Rotevatn, A., Tvedt, A.B., 2017. Techniques to determine the kinematics of synsedimentary normal faults and implications for fault growth models. Geological Society, London, Special Publications 439 (1), 187–217. https://doi.org/10.1144/SP439.22.

Kolawole, F., Phillips, T.B., Atekwana, E.A., Jackson, C.A.L., 2021. Structural inheritance controls strain distribution during early continental rifting, Rukwa Rift. Front. Earth Sci. 9, 707869. https://doi.org/10.3389/feart.2021.707869.

Kombrink, H., Doornenbal, J.C., Duin, E.J.T., den Dulk, M., ten Veen, J.H., Witmans, N., 2012. New insights into the geological structure of The Netherlands; results of a detailed mapping project. Neth. J. Geosci. 91 (4), 419–446. https://doi.org/10.1017/S0016774600000329.

Kley, J., Voigt, T., 2008. Late Cretaceous intraplate thrusting in central Europe: effect of Africa-Iberia-Europe convergence, not Alpine collision. Geology 36 (11), 839–842. https://doi.org/10.1130/G24930A.1.

Kley, J., 2018. Timing and spatial patterns of cretaceous and cenozoic inversion in the southern permian basin. Geological Society, London, Special Publications 469 (1), 19–31. https://doi.org/10.1144/SP469.12.

Kristensen, M.B., Childs, C.J., Korstgård, J.A., 2008. The 3D geometry of small-scale relay zones between normal faults in soft sediments. J. Struct. Geol. 30 (2), 257–272. https://doi.org/10.1016/j.jsg.2007.11.003.

Laó-Dávila, D.A., Al-Salmi, H.S., Abdelsalam, M.G., Atekwana, E.A., 2015. Hierarchical segmentation of the Malawi Rift: the influence of inherited lithospheric heterogeneity and kinematics in the evolution of continental rifts. Tectonics 34 (12), 2399–2417. https://doi.org/10.1002/2015TC003953.

Lăpădat, A., Imber, J., Yielding, G., Iacopini, D., McCaffrey, K.J., Long, J.J., Jones, R.R., 2017. Occurrence and Development of Folding Related to Normal Faulting within a Mechanically Heterogeneous Sedimentary Sequence: a Case Study from Inner Moray Firth, vol. 439. Geological Society, London, Special Publications, UK, pp. 373–394. https://doi.org/10.1144/SP439.18, 1.

Lowell, J.D., 1995. Mechanics of basin inversion from worldwide examples. Geological Society, London, Special Publications 88 (1), 39–57. https://doi.org/10.1144/GSL.SP.1995.088.01.04.

Manatschal, G., Lavier, L., Chenin, P., 2015. The role of inheritance in structuring hyperextended rift systems: some considerations based on observations and numerical modeling. Gondwana Res. 27 (1), 140–164. https://doi.org/10.1016/j.gr.2014.08.006.

Marchal, D., Guiraud, M., Rives, T., 2003. Geometric and morphologic evolution of normal fault planes and traces from 2D to 4D data. J. Struct. Geol. 25 (1), 135–158. https://doi.org/10.1016/S0191-8141(02)00011-1.

Michie, E.A.H., Braathen, A., 2024. How displacement analysis may aid fault risking strategies for CO2 storage. Basin Res. 36 (1), e12807. https://doi.org/10.1111/bre.12807.

Needham, D.T., Yielding, G., Freeman, B., 1996. Analysis of fault geometry and displacement patterns. Geological Society 99 (1), 189–199. https://doi.org/10.1144/GSL.SP.1996.099.01.15. London, Special Publications.

Nicol, A., Watterson, J., Walsh, J.J., Childs, C., 1996. The shapes, major axis orientations and displacement patterns of fault surfaces. J. Struct. Geol. 18 (2–3), 235–248. https://doi.org/10.1016/S0191-8141(96)80047-2.

Nicol, A., Gillespie, P.A., Childs, C., Walsh, J.J., 2002. Relay zones between mesoscopic thrust faults in layered sedimentary sequences. J. Struct. Geol. 24 (4), 709–727. https://doi.org/10.1016/S0191-8141(01)00113-4.

Nicol, A., Childs, C., Walsh, J.J., Manzocchi, T., Schöpfer, M.P.J., 2017. Interactions and growth of faults in an outcrop-scale system. Geological Society, London, Special Publications 439 (1), 23–39. https://doi.org/10.1144/SP439.9.

Nicol, A., Walsh, J., Childs, C., Manzocchi, T., 2020. The growth of faults. In: Tanner, D., Brandes, C. (Eds.), Understanding Faults. Elsevier Inc., pp. 221–255. https://doi.org/10.1016/B978-0-12-815985-9.00006-0

Nixon, C.W., Sanderson, D.J., Dee, S.J., Bull, J.M., Humphreys, R.J., Swanson, M.H., 2014. Fault interactions and reactivation within a normal-fault network at Milne Point, Alaska. AAPG (Am. Assoc. Pet. Geol.) Bull. 98 (10), 2081–2107. https://doi.org/10.1306/04301413177.

O'Sullivan, C.M., Childs, C.J., Saqab, M.M., Walsh, J.J., Shannon, P.M., 2022. Tectonostratigraphic evolution of the slyne basin. Solid Earth 13 (11), 1649–1671. https://doi.org/10.5194/se-13-1649-2022.

Osagiede, E.E., Rosenau, M., Rotevatn, A., Gawthorpe, R., Jackson, C.A.L., Rudolf, M., 2021. Influence of zones of pre-existing crustal weakness on strain localization and partitioning during rifting: insights from analog modeling using high-resolution 3D digital image correlation. Tectonics 40 (10), e2021TC006970. https://doi.org/10.1029/2021TC006970.

Peacock, D.C.P., Sanderson, D.J., 1991. Displacements, segment linkage and relay ramps in normal fault zones. J. Struct. Geol. 13 (6), 721–733. https://doi.org/10.1016/0191-8141(91)90033-F.

Pinto, L., Muñoz, C., Nalpas, T., Charrier, R., 2010. Role of sedimentation during basin inversion in analogue modelling. J. Struct. Geol. 32 (4), 554–565. https://doi.org/10.1016/j.jsg.2010.03.001.

Racero-Baena, A., Drake, S.J., 1996. Structural style and reservoir development in the West Netherlands oil province. In: Rondeel, H.E., Batjes, D.A.J., Nieuwenhuijs, W.H. (Eds.), Geology of Gas and Oil under the Netherlands. Springer, Netherlands, Dordrecht, pp. 211–227. https://doi.org/10.1007/978-94-009-0121-6_18.

Reilly, C., Nicol, A., Walsh, J., 2017. Importance of pre-existing fault size for the evolution of an inverted fault system. Geological Society, London, Special Publications 439 (1), 447–463. https://doi.org/10.1144/SP439.2.

Richetti, P.C., Zwaan, F., Schreurs, G., Schmitt, R.S., Schmid, T.C., 2023. Analogue modelling of basin inversion: implications for the Araripe Basin (Brazil). Solid Earth 14 (12), 1245–1266. https://doi.org/10.5194/se-14-1245-2023.

Rippon, J.H., 1984. Contoured patterns of the throw and hade of normal faults in the Coal Measures (Westphalian) of north-east Derbyshire. Proc. Yorks. Geol. Soc. 45 (3), 147–161. https://doi.org/10.1144/pygs.45.3.147.

Roche, V., Camanni, G., Childs, C., Manzocchi, T., Walsh, J., Conneally, J., Saqab, M.M., Delogkos, E., 2021. Variability in the three-dimensional geometry of segmented normal fault surfaces. Earth Sci. Rev. 216, 103523. https://doi.org/10.1016/j.earscirev.2021.103523.

Rotevatn, A., Jackson, C.A.L., Tvedt, A.B., Bell, R.E., Blækkan, I., 2019. How do normal faults grow? J. Struct. Geol. 125, 174–184. https://doi.org/10.1016/j.jsg.2018.08.005.

Seebeck, H., Tenthorey, E., Consoli, C., Nicol, A., 2015. Polygonal faulting and seal integrity in the Bonaparte Basin, Australia. Mar. Petrol. Geol. 60, 120–135. https://doi.org/10.1016/j.marpetgeo.2014.10.012.

TNO-GDN, 2024. Stratigraphic nomenclature of The Netherlands. https://www.dinoloket.nl/en/stratigraphic-nomenclature. (Accessed 26 September 2024).

Tondi, E., Cilona, A., Agosta, F., Aydin, A., Rustichelli, A., Renda, P., Giunta, G., 2012. Growth processes, dimensional parameters and scaling relationships of two conjugate sets of compactive shear bands in porous carbonate grainstones, Favignana Island, Italy. J. Struct. Geol. 37, 53–64. https://doi.org/10.1016/j.jsg.2012.02.003.

Torabi, A., Alaei, B., Libak, A., 2019. Normal fault 3D geometry and displacement revisited: insights from faults in the Norwegian Barents Sea. Mar. Petrol. Geol. 99, 135–155. https://doi.org/10.1016/j.marpetgeo.2018.09.032.

Tvedt, A.B., Rotevatn, A., Jackson, C.A.L., Fossen, H., Gawthorpe, R.L., 2013. Growth of normal faults in multilayer sequences: a 3D seismic case study from the Egersund Basin, Norwegian North Sea. J. Struct. Geol. 55, 1–20. https://doi.org/10.1016/j.jsg.2013.08.002.

van Adrichem Boogaert, H.A., Kouwe, W.P.F., 1993. Stratigraphic nomenclature of The Netherlands, revision and update by RGD and NOGEPA, TNO-NITG. Meded. Rijks Geol. Dienst.

van Balen, R.T., Van Bergen, F., De Leeuw, C., Pagnier, H., Simmelink, H., Van Wees, J.D., Verweij, J.M., 2000. Modelling the hydrocarbon generation and migration in the West Netherlands Basin, The Netherlands. Neth. J. Geosci. 79 (1), 29–44. https://doi.org/10.1017/S0016774600021557.

Vandycke, S., 2002. Palaeostress records in Cretaceous formations in NW Europe: extensional and strike–slip events in relationships with Cretaceous–Tertiary inversion tectonics. Tectonophysics 357 (1–4), 119–136. https://doi.org/10.1016/S0040-1951(02)00365-7.

van Wijhe, D.V., 1987. Structural evolution of inverted basins in the Dutch offshore. Tectonophysics 137 (1–4), 171–219. https://doi.org/10.1016/0040-1951(87)90320-9.

Vasey, D.A., Naliboff, J.B., Cowgill, E., Brune, S., Glerum, A., Zwaan, F., 2024. Impact of rift history on the structural style of intracontinental rift-inversion orogens. Geology 52 (6), 429–434. https://doi.org/10.1130/G51489.1.

Walsh, J.J., Watterson, J., 1988. Analysis of the relationship between displacements and dimensions of faults. J. Struct. Geol. 10 (3), 239–247. https://doi.org/10.1016/0191-8141(88)90057-0.

Walsh, J.J., Watterson, J., 1989. Displacement gradients on fault surfaces. J. Struct. Geol. 11 (3), 307–316. https://doi.org/10.1016/0191-8141(89)90070-9.

Walsh, J.J., Nicol, A., Childs, C., 2002. An alternative model for the growth of faults. J. Struct. Geol. 24 (11), 1669–1675. https://doi.org/10.1016/S0191-8141(01)00165-1.

Wang, L., Maestrelli, D., Corti, G., Zou, Y., Shen, C., 2021. Normal fault reactivation during multiphase extension: analogue models and application to the Turkana depression, East Africa. Tectonophysics 811, 228870. https://doi.org/10.1016/j.tecto.2021.228870.

Weert, A., Ogata, K., Vinci, F., Leo, C., Bertotti, G., Amory, J., Tavani, S., 2024. Multiple phase rifting and subsequent inversion in the West Netherlands Basin: implications for geothermal reservoir characterization. Solid Earth 15 (2), 121–141. https://doi.org/10.5194/se-15-121-2024.

Withjack, M.O., Henza, A.A., Schlische, R.W., 2017. Three-dimensional fault geometries and interactions within experimental models of multiphase extension. AAPG (Am. Assoc. Pet. Geol.) Bull. 101 (11), 1767–1789. https://doi.org/10.1306/02071716090.

Wong, T.E., Batjes, D.A.J., de Jager, J., 2007. Geology of the Netherlands. Royal Netherlands Academy of Arts and Sciences. Amsterdam.

Worum, G., Michon, L., 2005. Implications of continuous structural inversion in the West Netherlands Basin for understanding controls on Palaeogene deformation in NW Europe. Journal of the Geological society 162 (1), 73–85. https://doi.org/10.1144/0016-764904-011.

Worum, G., Michon, L., van Balen, R.T., van Wees, J.D., Cloetingh, S., Pagnier, H., 2005. Pre-Neogene controls on present-day fault activity in the West Netherlands Basin and Roer Valley Rift System (southern Netherlands): role of variations in fault orientation in a uniform low-stress regime. Quat. Sci. Rev. 24 (3–4), 473–488. https://doi.org/10.1016/j.quascirev.2004.02.020.

Worum, G., van Wees, J.D., 2017. High-resolution quantitative reconstruction of Late Cretaceous-Tertiary erosion in the West Netherlands Basin using multi-formation compaction trends and seismic data: implications for geothermal exploration. Acta Geodaetica et Geophysica 52 (2), 243–268. https://doi.org/10.1007/s40328-017-0196-6.

Ziegler, P.A., 1989. Geodynamic model for alpine intra-plate compressional deformation in western and central europe. Geological Society, London, Special Publications 44 (1), 63–85. https://doi.org/10.1144/GSL.SP.1989.044.01.05.

Ziegler, P.A., 1992. North Sea rift system. Tectonophysics 208 (1–3), 55–75. https://doi.org/10.1016/0040-1951(92)90336-5.

Zwaan, F., Schreurs, G., 2017. How oblique extension and structural inheritance influence rift segment interaction: insights from 4D analog models. Interpretation 5 (1), SD119–SD138. https://doi.org/10.1190/INT-2016-0063.1.

Zwaan, F., Chenin, P., Erratt, D., Manatschal, G., Schreurs, G., 2021. Complex rift patterns, a result of interacting crustal and mantle weaknesses, or multiphase rifting? Insights from analogue models. Solid Earth 12 (7), 1473–1495. https://doi.org/10.5194/se-12-1473-2021.

Zwaan, F., Schreurs, G., Buiter, S.J.H., Ferrer, O., Reitano, R., Rudolf, M., Willingshofer, E., 2022. Analogue modelling of basin inversion: a review and future perspectives. Solid Earth 13 (12), 1859–1905. https://doi.org/10.5194/se-13-1859-2022.